Measurement of the Inclusive Jet Cross Section at the Fermilab Tevatron $p\bar{p}$ Collider Using a Cone-Based Jet Algorithm

T. Aaltonen,[24] J. Adelman,[14] T. Akimoto,[56] M.G. Albrow,[18] B. Álvarez González,[12] S. Amerio[u],[44] D. Amidei,[35] A. Anastassov,[39] A. Annovi,[20] J. Antos,[15] G. Apollinari,[18] A. Apresyan,[49] T. Arisawa,[58] A. Artikov,[16] W. Ashmanskas,[18] A. Attal,[4] A. Aurisano,[54] F. Azfar,[43] P. Azzurri[s],[47] W. Badgett,[18] A. Barbaro-Galtieri,[29] V.E. Barnes,[49] B.A. Barnett,[26] V. Bartsch,[31] G. Bauer,[33] P.-H. Beauchemin,[34] F. Bedeschi,[47] P. Bednar,[15] D. Beecher,[31] S. Behari,[26] G. Bellettini[q],[47] J. Bellinger,[60] D. Benjamin,[17] A. Beretvas,[18] J. Beringer,[29] A. Bhatti,[51] M. Binkley,[18] D. Bisello[u],[44] I. Bizjak,[31] R.E. Blair,[2] C. Blocker,[7] B. Blumenfeld,[26] A. Bocci,[17] A. Bodek,[50] V. Boisvert,[50] G. Bolla,[49] D. Bortoletto,[49] J. Boudreau,[48] A. Boveia,[11] B. Brau,[11] A. Bridgeman,[25] L. Brigliadori,[44] C. Bromberg,[36] E. Brubaker,[14] J. Budagov,[16] H.S. Budd,[50] S. Budd,[25] K. Burkett,[18] G. Busetto[u],[44] P. Bussey[x],[22] A. Buzatu,[34] K. L. Byrum,[2] S. Cabrera[p],[17] C. Calancha,[32] M. Campanelli,[36] M. Campbell,[35] F. Canelli,[18] A. Canepa,[46] D. Carlsmith,[60] R. Carosi,[47] S. Carrillo[j],[19] S. Carron,[34] B. Casal,[12] M. Casarsa,[18] A. Castro[t],[6] P. Catastini[r],[47] D. Cauz[w],[55] V. Cavaliere[r],[47] M. Cavalli-Sforza,[4] A. Cerri,[29] L. Cerrito[n],[31] S.H. Chang,[28] Y.C. Chen,[1] M. Chertok,[8] G. Chiarelli,[47] G. Chlachidze,[18] F. Chlebana,[18] K. Cho,[28] D. Chokheli,[16] J.P. Chou,[23] G. Choudalakis,[33] S.H. Chuang,[53] K. Chung,[13] W.H. Chung,[60] Y.S. Chung,[50] C.I. Ciobanu,[45] M.A. Ciocci[r],[47] A. Clark,[21] D. Clark,[7] G. Compostella,[44] M.E. Convery,[18] J. Conway,[8] K. Copic,[35] M. Cordelli,[20] G. Cortiana[u],[44] D.J. Cox,[8] F. Crescioli[q],[47] C. Cuenca Almenar[p],[8] J. Cuevas[m],[12] R. Culbertson,[18] J.C. Cully,[35] D. Dagenhart,[18] M. Datta,[18] T. Davies,[22] P. de Barbaro,[50] S. De Cecco,[52] A. Deisher,[29] G. De Lorenzo,[4] M. Dell'Orso[q],[47] C. Deluca,[4] L. Demortier,[51] J. Deng,[17] M. Deninno,[6] P.F. Derwent,[18] G.P. di Giovanni,[45] C. Dionisi[v],[52] B. Di Ruzza[w],[55] J.R. Dittmann,[5] M. D'Onofrio,[4] S. Donati[q],[47] P. Dong,[9] J. Donini,[44] T. Dorigo,[44] S. Dube,[53] J. Efron,[40] A. Elagin,[54] R. Erbacher,[8] D. Errede,[25] S. Errede,[25] R. Eusebi,[18] H.C. Fang,[29] S. Farrington,[43] W.T. Fedorko,[14] R.G. Feild,[61] M. Feindt,[27] J.P. Fernandez,[32] C. Ferrazza[s],[47] R. Field,[19] G. Flanagan,[49] R. Forrest,[8] M. Franklin,[23] J.C. Freeman,[18] I. Furic,[19] M. Gallinaro,[52] J. Galyardt,[13] F. Garberson,[11] J.E. Garcia,[47] A.F. Garfinkel,[49] K. Genser,[18] H. Gerberich,[25] D. Gerdes,[35] A. Gessler,[27] S. Giagu[v],[52] V. Giakoumopoulou,[3] P. Giannetti,[47] K. Gibson,[48] J.L. Gimmell,[50] C.M. Ginsburg,[18] N. Giokaris,[3] M. Giordani[w],[55] P. Giromini,[20] M. Giunta[q],[47] G. Giurgiu,[26] V. Glagolev,[16] D. Glenzinski,[18] M. Gold,[38] N. Goldschmidt,[19] A. Golossanov,[18] G. Gomez,[12] G. Gomez-Ceballos,[33] M. Goncharov,[54] O. González,[32] I. Gorelov,[38] A.T. Goshaw,[17] K. Goulianos,[51] A. Gresele[u],[44] S. Grinstein,[23] C. Grosso-Pilcher,[14] R.C. Group,[18] U. Grundler,[25] J. Guimaraes da Costa,[23] Z. Gunay-Unalan,[36] C. Haber,[29] K. Hahn,[33] S.R. Hahn,[18] E. Halkiadakis,[53] B.-Y. Han,[50] J.Y. Han,[50] R. Handler,[60] F. Happacher,[20] K. Hara,[56] D. Hare,[53] M. Hare,[57] S. Harper,[43] R.F. Harr,[59] R.M. Harris,[18] M. Hartz,[48] K. Hatakeyama,[51] J. Hauser,[9] C. Hays,[43] M. Heck,[27] A. Heijboer,[46] B. Heinemann,[29] J. Heinrich,[46] C. Henderson,[33] M. Herndon,[60] J. Heuser,[27] S. Hewamanage,[5] D. Hidas,[17] C.S. Hill[c],[11] D. Hirschbuehl,[27] A. Hocker,[18] S. Hou,[1] M. Houlden,[30] S.-C. Hsu,[10] B.T. Huffman,[43] R.E. Hughes,[40] U. Husemann,[61] J. Huston,[36] J. Incandela,[11] G. Introzzi,[47] M. Iori[v],[52] A. Ivanov,[8] E. James,[18] B. Jayatilaka,[17] E.J. Jeon,[28] M.K. Jha,[6] S. Jindariani,[18] W. Johnson,[8] M. Jones,[49] K.K. Joo,[28] S.Y. Jun,[13] J.E. Jung,[28] T.R. Junk,[18] T. Kamon,[54] D. Kar,[19] P.E. Karchin,[59] Y. Kato,[42] R. Kephart,[18] J. Keung,[46] V. Khotilovich,[54] B. Kilminster,[40] D.H. Kim,[28] H.S. Kim,[28] J.E. Kim,[28] M.J. Kim,[20] S.B. Kim,[28] S.H. Kim,[56] Y.K. Kim,[14] N. Kimura,[56] L. Kirsch,[7] S. Klimenko,[19] B. Knuteson,[33] B.R. Ko,[17] S.A. Koay,[11] K. Kondo,[58] D.J. Kong,[28] J. Konigsberg,[19] A. Korytov,[19] A.V. Kotwal,[17] M. Kreps,[27] J. Kroll,[46] D. Krop,[14] N. Krumnack,[5] M. Kruse,[17] V. Krutelyov,[11] T. Kubo,[56] T. Kuhr,[27] N.P. Kulkarni,[59] M. Kurata,[56] Y. Kusakabe,[58] S. Kwang,[14] A.T. Laasanen,[49] S. Lami,[47] S. Lammel,[18] M. Lancaster,[31] R.L. Lander,[8] K. Lannon,[40] A. Lath,[53] G. Latino[r],[47] I. Lazzizzera[u],[44] T. LeCompte,[2] E. Lee,[54] S.W. Lee[o],[54] S. Leone,[47] J.D. Lewis,[18] C.S. Lin,[29] J. Linacre,[43] M. Lindgren,[18] E. Lipeles,[10] A. Lister,[8] D.O. Litvintsev,[18] C. Liu,[48] T. Liu,[18] N.S. Lockyer,[46] A. Loginov,[61] M. Loreti[u],[44] L. Lovas,[15] R.-S. Lu,[1] D. Lucchesi[u],[44] J. Lueck,[27] C. Luci[v],[52] P. Lujan,[29] P. Lukens,[18] G. Lungu,[51] L. Lyons,[43] J. Lys,[29] R. Lysak,[15] E. Lytken,[49] P. Mack,[27] D. MacQueen,[34] R. Madrak,[18] K. Maeshima,[18] K. Makhoul,[33] T. Maki,[24] P. Maksimovic,[26] S. Malde,[43] S. Malik,[31] G. Manca,[30] A. Manousakis-Katsikakis,[3] F. Margaroli,[49] C. Marino,[27] C.P. Marino,[25] A. Martin,[61] V. Martin[i],[22] M. Martínez,[4] R. Martínez-Ballarín,[32] T. Maruyama,[56] P. Mastrandrea,[52] T. Masubuchi,[56] M.E. Mattson,[59] P. Mazzanti,[6] K.S. McFarland,[50] P. McIntyre,[54] R. McNulty[h],[30] A. Mehta,[30] P. Mehtala,[24] A. Menzione,[47] P. Merkel,[49] C. Mesropian,[51] T. Miao,[18] N. Miladinovic,[7] R. Miller,[36] C. Mills,[23] M. Milnik,[27] A. Mitra,[1] G. Mitselmakher,[19] H. Miyake,[56] N. Moggi,[6] C.S. Moon,[28] R. Moore,[18] M.J. Morello[q],[47] J. Morlok,[27] P. Movilla Fernandez,[18] J. Mülmenstädt,[29] A. Mukherjee,[18] Th. Muller,[27] R. Mumford,[26] P. Murat,[18] M. Mussini[t],[6] J. Nachtman,[18] Y. Nagai,[56] A. Nagano,[56] J. Naganoma,[58] K. Nakamura,[56] I. Nakano,[41]

A. Napier,[57] V. Necula,[17] C. Neu,[46] M.S. Neubauer,[25] J. Nielsen,[e,29] L. Nodulman,[2] M. Norman,[10]
O. Norniella,[25] E. Nurse,[31] L. Oakes,[43] S.H. Oh,[17] Y.D. Oh,[28] I. Oksuzian,[19] T. Okusawa,[42] R. Orava,[24]
K. Osterberg,[24] S. Pagan Griso,[u,44] C. Pagliarone,[47] E. Palencia,[18] V. Papadimitriou,[18] A. Papaikonomou,[27]
A.A. Paramonov,[14] B. Parks,[40] S. Pashapour,[34] J. Patrick,[18] G. Pauletta,[w,55] M. Paulini,[13] C. Paus,[33] D.E. Pellett,[8]
A. Penzo,[55] T.J. Phillips,[17] G. Piacentino,[47] E. Pianori,[46] L. Pinera,[19] K. Pitts,[25] C. Plager,[9] L. Pondrom,[60]
O. Poukhov*,[16] N. Pounder,[43] F. Prakoshyn,[16] A. Pronko,[18] J. Proudfoot,[2] F. Ptohos,[g,18] E. Pueschel,[13]
G. Punzi,[q,47] J. Pursley,[60] J. Rademacker,[c,43] A. Rahaman,[48] V. Ramakrishnan,[60] N. Ranjan,[49] I. Redondo,[32]
B. Reisert,[18] V. Rekovic,[38] P. Renton,[43] M. Rescigno,[52] S. Richter,[27] F. Rimondi,[t,6] L. Ristori,[47] A. Robson,[22]
T. Rodrigo,[12] T. Rodriguez,[46] E. Rogers,[25] S. Rolli,[57] R. Roser,[18] M. Rossi,[55] R. Rossin,[11] P. Roy,[34] A. Ruiz,[12]
J. Russ,[13] V. Rusu,[18] H. Saarikko,[24] A. Safonov,[54] W.K. Sakumoto,[50] O. Saltó,[4] L. Santi,[w,55] S. Sarkar,[v,52]
L. Sartori,[47] K. Sato,[18] A. Savoy-Navarro,[45] T. Scheidle,[27] P. Schlabach,[18] A. Schmidt,[27] E.E. Schmidt,[18]
M.A. Schmidt,[14] M.P. Schmidt†,[61] M. Schmitt,[39] T. Schwarz,[8] L. Scodellaro,[12] A.L. Scott,[11] A. Scribano,[r,47]
F. Scuri,[47] A. Sedov,[49] S. Seidel,[38] Y. Seiya,[42] A. Semenov,[16] L. Sexton-Kennedy,[18] A. Sfyrla,[21] S.Z. Shalhout,[59]
T. Shears,[30] P.F. Shepard,[48] D. Sherman,[23] M. Shimojima,[l,56] S. Shiraishi,[14] M. Shochet,[14] Y. Shon,[60] I. Shreyber,[37]
A. Sidoti,[47] P. Sinervo,[34] A. Sisakyan,[16] A.J. Slaughter,[18] J. Slaunwhite,[40] K. Sliwa,[57] J.R. Smith,[8] F.D. Snider,[18]
R. Snihur,[34] A. Soha,[8] S. Somalwar,[53] V. Sorin,[36] J. Spalding,[18] T. Spreitzer,[34] P. Squillacioti,[r,47]
M. Stanitzki,[61] R. St. Denis,[22] B. Stelzer,[9] O. Stelzer-Chilton,[43] D. Stentz,[39] J. Strologas,[38] D. Stuart,[11]
J.S. Suh,[28] A. Sukhanov,[19] I. Suslov,[16] T. Suzuki,[56] A. Taffard,[d,25] R. Takashima,[41] Y. Takeuchi,[56] R. Tanaka,[41]
M. Tecchio,[35] P.K. Teng,[1] K. Terashi,[51] J. Thom,[f,18] A.S. Thompson,[22] G.A. Thompson,[25] E. Thomson,[46]
P. Tipton,[61] V. Tiwari,[13] S. Tkaczyk,[18] D. Toback,[54] S. Tokar,[15] K. Tollefson,[36] T. Tomura,[56] D. Tonelli,[18]
S. Torre,[20] D. Torretta,[18] P. Totaro,[w,55] S. Tourneur,[45] Y. Tu,[46] N. Turini,[r,47] F. Ukegawa,[56] S. Vallecorsa,[21]
N. van Remortel,[a,24] A. Varganov,[35] E. Vataga,[s,47] F. Vázquez,[j,19] G. Velev,[18] C. Vellidis,[3] V. Veszpremi,[49]
M. Vidal,[32] R. Vidal,[18] I. Vila,[12] R. Vilar,[12] T. Vine,[31] M. Vogel,[38] I. Volobouev,[o,29] G. Volpi,[q,47] F. Würthwein,[10]
P. Wagner,[2] R.G. Wagner,[2] R.L. Wagner,[18] J. Wagner-Kuhr,[27] W. Wagner,[27] T. Wakisaka,[42] R. Wallny,[9]
S.M. Wang,[1] A. Warburton,[34] D. Waters,[31] M. Weinberger,[54] W.C. Wester III,[18] B. Whitehouse,[57] D. Whiteson,[d,46]
A.B. Wicklund,[2] E. Wicklund,[18] G. Williams,[34] H.H. Williams,[46] P. Wilson,[18] B.L. Winer,[40] P. Wittich,[f,18]
S. Wolbers,[18] C. Wolfe,[14] T. Wright,[35] X. Wu,[21] S.M. Wynne,[30] A. Yagil,[10] K. Yamamoto,[42] J. Yamaoka,[53]
U.K. Yang,[k,14] Y.C. Yang,[28] W.M. Yao,[29] G.P. Yeh,[18] J. Yoh,[18] K. Yorita,[14] T. Yoshida,[42] G.B. Yu,[50] I. Yu,[28]
S.S. Yu,[18] J.C. Yun,[18] L. Zanello,[v,52] A. Zanetti,[55] I. Zaw,[23] X. Zhang,[25] Y. Zheng,[b,9] and S. Zucchelli[t,6]

(CDF Collaboration‡)

[1]*Institute of Physics, Academia Sinica, Taipei, Taiwan 11529, Republic of China*
[2]*Argonne National Laboratory, Argonne, Illinois 60439*
[3]*University of Athens, 157 71 Athens, Greece*
[4]*Institut de Fisica d'Altes Energies, Universitat Autonoma de Barcelona, E-08193, Bellaterra (Barcelona), Spain*
[5]*Baylor University, Waco, Texas 76798*
[6]*Istituto Nazionale di Fisica Nucleare Bologna, [t]University of Bologna, I-40127 Bologna, Italy*
[7]*Brandeis University, Waltham, Massachusetts 02254*
[8]*University of California, Davis, Davis, California 95616*
[9]*University of California, Los Angeles, Los Angeles, California 90024*
[10]*University of California, San Diego, La Jolla, California 92093*
[11]*University of California, Santa Barbara, Santa Barbara, California 93106*
[12]*Instituto de Fisica de Cantabria, CSIC-University of Cantabria, 39005 Santander, Spain*
[13]*Carnegie Mellon University, Pittsburgh, PA 15213*
[14]*Enrico Fermi Institute, University of Chicago, Chicago, Illinois 60637*
[15]*Comenius University, 842 48 Bratislava, Slovakia; Institute of Experimental Physics, 040 01 Kosice, Slovakia*
[16]*Joint Institute for Nuclear Research, RU-141980 Dubna, Russia*
[17]*Duke University, Durham, North Carolina 27708*
[18]*Fermi National Accelerator Laboratory, Batavia, Illinois 60510*
[19]*University of Florida, Gainesville, Florida 32611*
[20]*Laboratori Nazionali di Frascati, Istituto Nazionale di Fisica Nucleare, I-00044 Frascati, Italy*
[21]*University of Geneva, CH-1211 Geneva 4, Switzerland*
[22]*Glasgow University, Glasgow G12 8QQ, United Kingdom*
[23]*Harvard University, Cambridge, Massachusetts 02138*
[24]*Division of High Energy Physics, Department of Physics,*
University of Helsinki and Helsinki Institute of Physics, FIN-00014, Helsinki, Finland
[25]*University of Illinois, Urbana, Illinois 61801*
[26]*The Johns Hopkins University, Baltimore, Maryland 21218*
[27]*Institut für Experimentelle Kernphysik, Universität Karlsruhe, 76128 Karlsruhe, Germany*

[28] Center for High Energy Physics: Kyungpook National University,
Daegu 702-701, Korea; Seoul National University, Seoul 151-742,
Korea; Sungkyunkwan University, Suwon 440-746,
Korea; Korea Institute of Science and Technology Information, Daejeon,
305-806, Korea; Chonnam National University, Gwangju, 500-757, Korea
[29] Ernest Orlando Lawrence Berkeley National Laboratory, Berkeley, California 94720
[30] University of Liverpool, Liverpool L69 7ZE, United Kingdom
[31] University College London, London WC1E 6BT, United Kingdom
[32] Centro de Investigaciones Energeticas Medioambientales y Tecnologicas, E-28040 Madrid, Spain
[33] Massachusetts Institute of Technology, Cambridge, Massachusetts 02139
[34] Institute of Particle Physics: McGill University, Montréal,
Canada H3A 2T8; and University of Toronto, Toronto, Canada M5S 1A7
[35] University of Michigan, Ann Arbor, Michigan 48109
[36] Michigan State University, East Lansing, Michigan 48824
[37] Institution for Theoretical and Experimental Physics, ITEP, Moscow 117259, Russia
[38] University of New Mexico, Albuquerque, New Mexico 87131
[39] Northwestern University, Evanston, Illinois 60208
[40] The Ohio State University, Columbus, Ohio 43210
[41] Okayama University, Okayama 700-8530, Japan
[42] Osaka City University, Osaka 588, Japan
[43] University of Oxford, Oxford OX1 3RH, United Kingdom
[44] Istituto Nazionale di Fisica Nucleare, Sezione di Padova-Trento, [u] University of Padova, I-35131 Padova, Italy
[45] LPNHE, Universite Pierre et Marie Curie/IN2P3-CNRS, UMR7585, Paris, F-75252 France
[46] University of Pennsylvania, Philadelphia, Pennsylvania 19104
[47] Istituto Nazionale di Fisica Nucleare Pisa, [q] University of Pisa,
[r] University of Siena and [s] Scuola Normale Superiore, I-56127 Pisa, Italy
[48] University of Pittsburgh, Pittsburgh, Pennsylvania 15260
[49] Purdue University, West Lafayette, Indiana 47907
[50] University of Rochester, Rochester, New York 14627
[51] The Rockefeller University, New York, New York 10021
[52] Istituto Nazionale di Fisica Nucleare, Sezione di Roma 1,
[v] Sapienza Università di Roma, I-00185 Roma, Italy
[53] Rutgers University, Piscataway, New Jersey 08855
[54] Texas A&M University, College Station, Texas 77843
[55] Istituto Nazionale di Fisica Nucleare Trieste/ Udine, [w] University of Trieste/ Udine, Italy
[56] University of Tsukuba, Tsukuba, Ibaraki 305, Japan
[57] Tufts University, Medford, Massachusetts 02155
[58] Waseda University, Tokyo 169, Japan
[59] Wayne State University, Detroit, Michigan 48201
[60] University of Wisconsin, Madison, Wisconsin 53706
[61] Yale University, New Haven, Connecticut 06520
(Dated: August 11, 2008)

We present a measurement of the inclusive jet cross section in $p\bar{p}$ collisions at $\sqrt{s} = 1.96$ TeV based on data collected by the CDF II detector with an integrated luminosity of 1.13 fb^{-1}. The measurement was made using the cone-based Midpoint jet clustering algorithm in the rapidity region of $|y| < 2.1$. The results are consistent with next-to-leading-order perturbative QCD predictions based on recent parton distribution functions (PDFs), and are expected to provide increased precision in PDFs at high parton momentum fraction x. The results are also compared to the recent inclusive jet cross section measurement using the k_T jet clustering algorithm, and we find that the ratio of the cross sections measured with the two algorithms is in agreement with theoretical expectations over a large range of jet transverse momentum and rapidity.

[*] Deceased
[†] Deceased
[‡] With visitors from [a] Universiteit Antwerpen, B-2610 Antwerp, Belgium, [b] Chinese Academy of Sciences, Beijing 100864, China, [c] University of Bristol, Bristol BS8 1TL, United Kingdom,

[d] University of California Irvine, Irvine, CA 92697, [e] University of California Santa Cruz, Santa Cruz, CA 95064, [f] Cornell University, Ithaca, NY 14853, [g] University of Cyprus, Nicosia CY-1678, Cyprus, [h] University College Dublin, Dublin 4, Ireland, [i] University of Edinburgh, Edinburgh EH9 3JZ, United Kingdom, [j] Universidad

I. INTRODUCTION

The measurement of the differential inclusive jet cross section at the Fermilab Tevatron probes the highest momentum transfers in particle collisions currently attainable in any accelerator experiment, and thus is potentially sensitive to new physics such as quark substructure [1, 2]. The measurement also provides a direct test of predictions of perturbative quantum chromodynamics (pQCD) [3–5]. The inclusive jet cross section measurements at Tevatron Run II [6–9] cover up to 600 GeV/c in jet transverse momentum p_T [10], and range over more than eight orders of magnitude in differential cross section. Comparisons of the measured cross section with pQCD predictions provide constraints on the parton distribution function (PDF) of the (anti)proton, in particular at high momentum fraction x ($x \gtrsim 0.3$) where the gluon distribution is poorly constrained [11]. Further constraints on the gluon distribution at high x will contribute to reduced uncertainties on theoretical predictions of many interesting physics processes both for experiments at the Tevatron and for future experiments at the Large Hadron Collider (LHC). One example is $t\bar{t}$ production at the Tevatron for which the dominant PDF uncertainty arises from the uncertainty in the high-x gluon distribution. In addition, searches for new physics beyond the standard model at high p_T such as quark substructure require precise knowledge of PDFs at high x.

Jets are defined by algorithms which cluster together objects such as energies measured in calorimeter towers, particles, or partons. Jet clustering relies on the association of objects based either on proximity in coordinate space (as in cone algorithms) or in momentum space (as in k_T algorithms) [12–15]. The CDF Collaboration recently published a measurement of the inclusive jet cross section in the rapidity region $0.1 < |y| < 0.7$ [10] using a cone-based jet clustering algorithm [16] based on 0.39 fb^{-1} of the Run II data [6]. This paper presents an updated measurement based on 1.13 fb^{-1} with the kinematic range extended up to $|y| = 2.1$, and comparisons with next-to-leading-order (NLO) pQCD predictions based on recent PDFs of the proton [11, 17]. The extension of the rapidity range significantly increases kinematic reach in $x - Q$ space, where Q denotes the momentum transfer, and helps to further constrain the proton PDFs. The D0 Collaboration also recently reported a measurement of the inclusive jet cross section using 0.70 fb^{-1} of data in the rapidity region $|y| < 2.4$ [9].

Similar measurements of the inclusive jet cross sec-

tion have been made by the CDF Collaboration in Run II using the k_T jet clustering algorithm [18] in the region of $0.1 < |y| < 0.7$ [7] and later in the region up to $|y| = 2.1$ [8]. The k_T algorithm has been used successfully at e^+e^- and $e^\pm p$ collider experiments; however, the cone algorithms have been used traditionally at hadron collider experiments, mainly due to the associated simplicity in constructing corrections for the underlying event and for multiple interactions in the same bunch crossing [12]. It is worth noting that previous measurements made at the Tevatron in Run I using a cone algorithm and k_T algorithm showed only marginal agreement [19, 20].

The rest of this paper proceeds as follows: Section II describes the CDF detector components most relevant to this analysis. The details of the jet clustering algorithm and the data sample used in this measurement are presented in Secs. III and IV. Section V explains the methods used to correct the CDF data for all detector effects, so that the measured cross section may be directly compared to theoretical predictions. The event samples from Monte Carlo (MC) event generators and CDF detector simulation that are used to derive these corrections are also discussed in this section. Systematic uncertainties in the cross section measurement are discussed in Sec. VI. Section VII discusses NLO pQCD predictions on the inclusive jet cross sections, and Sec. VIII presents the measured cross sections and comparisons to those predictions. In Sec. IX the measured cross sections are also compared to the recent measurement using the k_T jet clustering algorithm [8], and in Sec. X conclusions are presented.

II. THE CDF II DETECTOR

The CDF II detector, shown schematically in Fig. 1, is described in detail elsewhere [21]. Here, those components that are relevant to this measurement are briefly described. The central detector consists of a silicon vertex detector (SVXII) [22] and intermediate silicon layers (ISL) [23], covering the radial ranges of $1.5 - 11$ cm and $19 - 30$ cm, respectively. They are located inside a cylindrical open-cell drift chamber [24] of 96 layers organized in 8 superlayers with alternating structures of axial and $\pm 2°$ stereo readout within a radial range between 40 and 137 cm. The tracking system is located inside a superconducting solenoid magnet which provides an axial 1.4 T magnetic field. Surrounding the magnet coil are projective-tower-geometry sampling calorimeters to measure the energy of interacting particles.

The central calorimeter covers the region of $|\eta| < 1.1$ and is divided into two halves at $|\eta| = 0$. It consists of 48 modules, segmented into towers of granularity $\Delta\eta \times \Delta\phi \approx 0.1 \times 0.26$. The central electromagnetic calorimeter (CEM) [25, 26] consists of lead-scintillator with a depth of about 18 radiation lengths; the central hadron calorimeter (CHA) [27] consists of iron-scintillator with a depth of approximately 4.7 in-

Iberoamericana, Mexico D.F., Mexico, ^{k}University of Manchester, Manchester M13 9PL, England, ^{l}Nagasaki Institute of Applied Science, Nagasaki, Japan, ^{m}University de Oviedo, E-33007 Oviedo, Spain, ^{n}Queen Mary, University of London, London, E1 4NS, England, ^{o}Texas Tech University, Lubbock, TX 79409, ^{p}IFIC(CSIC-Universitat de Valencia), 46071 Valencia, Spain, ^{x}Royal Society of Edinburgh/Scottish Executive Support Research Fellow,

teraction lengths. The energy resolution of the CEM for electrons is $\sigma(E_T)/E_T = 13.5\%/\sqrt{E_T(\text{GeV})} \oplus 1.5\%$, while the energy resolution of the CHA for charged pions that do not interact in the CEM is $\sigma(E_T)/E_T = 50\%/\sqrt{E_T(\text{GeV})} \oplus 3\%$.

The forward region, $1.1 < |\eta| < 3.6$, is covered by the plug calorimeters [28, 29] consisting of lead-scintillator for the electromagnetic section (PEM) and iron-scintillator for the hadronic section (PHA). The PEM and PHA have a depth of about 23.2 radiation lengths and 6.8 interaction lengths, respectively. The PEM and PHA are identically segmented into 480 towers of sizes which vary with η ($\Delta\eta \times \Delta\phi \approx 0.1 \times 0.13$ at $|\eta| < 1.8$ and $\Delta\eta \times \Delta\phi \approx 0.6 \times 0.26$ at $|\eta| = 3.6$). The energy resolution of the PEM for electrons is $\sigma(E_T)/E_T = 14\%/\sqrt{E_T(\text{GeV})} \oplus 1\%$, while the energy resolution of the PHA for charged pions that do not interact in the PEM is $\sigma(E_T)/E_T = 74\%\sqrt{E_T(\text{GeV})} \oplus 4\%$. The gap in the projective tower geometry between CHA and PHA, corresponding to $0.7 < |\eta| < 1.3$, is covered by an iron-scintillator endwall hadron calorimeter (WHA) [27] with segmentation similar to that of the central calorimeter. The WHA has a depth of approximately 4.5 interaction lengths, and a resolution of $\sigma(E_T)/E_T = 75\%/\sqrt{E_T(\text{GeV})} \oplus 4\%$ for charged pions that do not interact in the electromagnetic section.

A system of Cherenkov luminosity counters (CLC) [30] is located around the beampipe and inside the plug calorimeters. The CLC detector, covering the range $3.6 < |\eta| < 4.6$, consists of two modules on the two sides of the interaction region. Each module consists of 48 thin and long gas Cherenkov counters arranged in three concentric layers of 16 counters. The CLC detector is used to measure the number of inelastic $p\bar{p}$ collisions per bunch crossing and thereby the luminosity.

III. JET CLUSTERING

The definition of a jet is a fundamental step in the measurement of the inclusive jet cross section. Jets are collimated sprays of particles originating from quark or gluon fragmentation. They must be defined by clustering algorithms, and the algorithms are designed such that the jets clustered from the complex structure of objects (such as energies measured in calorimeter towers) in each event represent the physical properties of the partons from the hard scattering. The commonly-used jet clustering algorithms can be categorized into two classes, *i.e.*, cone-based algorithms and k_T algorithms. The two categories of algorithms have different strengths and weaknesses in regards to comparisons between data and theoretical predictions. For example, as mentioned previously, the underlying event and multiple interaction corrections are simpler for cone algorithms, while k_T algorithms have a smaller sensitivity to higher order perturbative QCD effects [12–14].

The k_T algorithms are based on pair-wise succes-sive combinations. In the k_T algorithm [18], initially each object to be clustered is considered as a proto-jet, and the quantities $k_{T,i}^2 = p_{T,i}^2$ and $k_{T,(i,j)}^2 = \min(p_{T,i}^2, p_{T,j}^2)\Delta R_{i,j}^2/D^2$ are then computed for each proto-jet and each pair of proto-jets, respectively, where $p_{T,i}$ is the p_T of the i-th proto-jet, $\Delta R_{i,j}$ is the distance in a specified coordinate space (*e.g.*, $y - \phi$ space) between each pair of proto-jets, and D is the parameter that controls the size of the jet. If the smallest of these quantities is a $k_{T,i}^2$, that proto-jet becomes a jet and is removed from the list of proto-jets, and if the smallest quantity is a $k_{T,(i,j)}^2$, the two proto-jets are merged into a single proto-jet and the original two proto-jets are removed from the proto-jet list. This process is iterated until all the proto-jets become jets.

In cone algorithms, objects in a cone in a specified coordinate space are clustered, and the axis of the cone is required to coincide with the direction of the cone defined by a sum of all objects inside the cone. Such cones are referred to as stable cones, and jets are formed from these stable cones. Cone algorithms used in experiments so far search for stable cones only from the locations of seeds, objects above a threshold, in order to keep the CPU running time manageable. The use of seeds makes these cone algorithms sensitive to soft particles, and it has been pointed out that pQCD calculations with cone algorithms used previously in Run I [19, 31] may face difficulties due to the presence of infrared singularities [12, 32]. The Midpoint cone-based jet clustering algorithm [12] used in this paper and also in other recent measurements [6, 9] reduces this problem by placing additional seeds at the midpoint between stable cones having a separation of less than twice the clustering cone radius. More details of the Midpoint jet clustering algorithm used in this measurement are described below.

First, a list of objects to be clustered needs to be identified. In this paper, jets are clustered at three different levels. The list of objects to be clustered is different in each case:

(a) Detector level (in data or MC events after detector simulation): CDF reconstructs jets from four-vectors associated with calorimeter towers. The four-vector associated with each tower is defined as a sum of vectors for the electromagnetic and hadronic sections. The vector of each section is defined as a massless four-vector with magnitude equal to the deposited energy and with direction from the primary interaction event vertex to the center of each section. To reduce the effect of detector noise, only towers with $p_T > 100$ MeV/c are included in the list.

(b) Hadron level (in MC events): four-vectors of the stable particles (mostly hadrons and photons from π^0 decays) [33] are the basic elements to be clustered.

(c) Parton level (in MC events or NLO pQCD the-

ory): four-vectors of partons are used to form parton-level jets. In MC events, the partons before hadronization are used, and in the pQCD theory, the partons after all QCD radiation are used. There are at most three partons in the list in the NLO pQCD theory used in this paper.

Then, a list of seed objects is made with the requirement that the p_T of the object exceeds a fixed threshold, which is set to 1 GeV/c in this analysis. At each seed location a cone of radius $R_{\mathrm{cone}} = 0.7$ in $y - \phi$ space is constructed, and the four-momentum vectors of all objects located in the cone are summed. This four-vector sum defines the *centroid* of the cluster, *i.e.*,

$$
\begin{aligned}
p^{\mathrm{cluster}} &= (E^{\mathrm{cluster}}, \mathbf{p}^{\mathrm{cluster}}) = \sum_{i \in \mathrm{cone}} (E^i, p_x^i, p_y^i, p_z^i), \\
p_T^{\mathrm{cluster}} &= \sqrt{(p_x^{\mathrm{cluster}})^2 + (p_y^{\mathrm{cluster}})^2}, \\
y^{\mathrm{cluster}} &= \frac{1}{2} \ln \left(\frac{E^{\mathrm{cluster}} + p_z^{\mathrm{cluster}}}{E^{\mathrm{cluster}} - p_z^{\mathrm{cluster}}} \right), \\
\phi^{\mathrm{cluster}} &= \tan^{-1} \left(p_y^{\mathrm{cluster}} / p_x^{\mathrm{cluster}} \right).
\end{aligned}
\tag{1}
$$

This definition for the kinematics of a cluster is referred to as the four-vector recombination scheme [12]. The four-vector of the cluster is then used as a new cone axis. From this axis a new cone is drawn and the process of summing up the four-vectors of all objects in the cone is repeated. This process is iterated until the cone axis and the centroid coincide, indicating that a stable cone has been formed.

In the next step in the algorithm, additional seeds are added at the midpoints between all pairs of stable cones whose separation in $y - \phi$ space is less than $2R_{\mathrm{cone}}$. A cone of radius R_{cone} is then drawn around the midpoint seed and is used to form a stable cone. If the resulting cone is not already in the list of stable cones, it is added to the list. After all midpoint seeds have been explored, the list of stable cones is complete. As mentioned earlier, the use of these additional seeds reduces the sensitivity of the algorithm to soft particles and makes this algorithm infrared safe up to NLO in pQCD for inclusive jet cross sections.

It is possible that stable cones overlap, *i.e.*, an object may be contained in more than one stable cone. To resolve these configurations, a split-and-merge algorithm is employed. After stable cones are sorted in decreasing p_T, overlapping stable cones are merged if the p_T of the four-vector sum of shared objects between two overlapping cones is more than a fraction, $f_{\mathrm{merge}} = 0.75$, of the p_T of the lower-p_T cone; otherwise, the shared objects are assigned to the cone closer in $y - \phi$ space. After cone overlaps are resolved and all objects are uniquely assigned to a cluster, the resulting clusters are promoted to jets and their kinematic properties are determined using the four-vector recombination scheme as defined in Eq. (1) where the sum is over all objects assigned to the jet. The Midpoint algorithm used in this measurement may then be summarized as follows:

(1) A list of seeds which includes only objects with $p_T > 1$ GeV/c is made.

(2) Stable cones with radius $R_{\mathrm{cone}} = 0.7$ are constructed around each seed.

(3) An additional seed is added at the midpoint between each pair of stable cones separated by less than $2R_{\mathrm{cone}}$. Each additional seed is used to search for stable cones that have not already been found.

(4) The stable cones are p_T-ordered and the split-and-merge procedure is performed to resolve overlapping cones.

IV. DATA SAMPLE AND EVENT SELECTION

The measurement described in this paper is based on the data taken from February 2002 until February 2006 corresponding to an integrated luminosity of 1.13 ± 0.07 fb^{-1}. The data samples used in this measurement were collected using four paths in the CDF three-level trigger system. The level-1 trigger requires a calorimeter trigger tower, consisting of a specific pair of calorimeter towers adjacent in η, to have $E_T > 5, 5, 10,$ and 10 GeV in the four trigger paths, respectively, for most of the time; however, the E_T threshold for the last path is changed from 10 to 20 GeV in the course of the data-taking period in order to accomodate the increase in the trigger rate due to increasing instantaneous luminosity. At level 2, the calorimeter towers are clustered using a nearest-neighbor algorithm. Events are required to have at least one level-2 trigger cluster with $E_T > 15, 40, 60,$ and 90 GeV in each of four trigger paths, respectively. Events in these four paths are further required to have at least one jet with $E_T > 20, 50, 70,$ and 100 GeV at level 3, where the jet clustering is performed using the CDF Run I cone algorithm with a cone radius $R_{\mathrm{cone}} = 0.7$ [31]. These four jet trigger paths are referred to as "jet20", "jet50", "jet70" and "jet100" hereafter. The minimum p_T at which jets from a given trigger path are used is determined by requiring a trigger efficiency greater than 99.5%. The trigger efficiencies in the region $0.1 < |y| < 0.7$ are shown in Fig. 2.

The jet20, jet50, and jet70 triggers are artificially reduced (prescaled) in order to avoid saturating the bandwidth of the trigger and data acquisition system. The jet70 trigger is prescaled by a constant factor of 8 for all data used in this measurement, which means that only one event in eight satisfying the trigger requirements is accepted. The prescales for the jet20 and jet50 triggers were changed during the period this data sample was acquired in order to accommodate increasing instantaneous luminosity. The integrated luminosities of the jet50 and jet20 trigger data samples corrected for the prescale factors are 31.9 and 1.4 pb^{-1}, respectively. The four jet triggers are summarized in Table I. The jet yield distributions as functions of uncorrected jet p_T (p_T^{CAL}) [34] in

TABLE I: Summary of the jet triggers used in this measurement. For each dataset, the E_T threshold on the trigger towers at level 1, calorimeter clusters at level 2 and jets clustered at level 3, and the corresponding prescale factors are shown. When multiple numbers are shown in a single column, it means the prescale factor or the E_T threshold changed during the data taking period studied.

Dataset	level-1		level-2		level-3		Combined
	E_T (GeV)	Prescale	E_T (GeV)	Prescale	E_T (GeV)	Prescale	Prescale
jet20	5	20,50	15	12,25	20	1	808
jet50	5	20,50	40	1,5	50	1	35
jet70	10	1,8	60	8,1	70	1	8
jet100	10,20	1	90	1	100	1	1

the rapidity region $0.1 < |y| < 0.7$ before correcting for trigger prescales are shown in Fig. 3.

Cosmic ray and beam-related background events are removed by applying a cut on missing-E_T significance, $\not{E}_T/\sqrt{\sum E_T}$ [35]. The cut threshold varies with the highest-p_T jet in the event and is defined by:

$$\not{E}_T/\sqrt{\sum E_T} < \min(3 + 0.0125 \times p_T^{\max}, 6); \quad (2)$$

where $p_T^{\max}$ is the maximum uncorrected jet p_T in the event in units of GeV/c, and E_T and $\not{E}_T$ are in units of GeV. The missing-E_T significance cut is about 100% efficient for low-p_T jets, and the acceptance decreases to about 90% for the highest-p_T jets used in this measurement.

Primary vertices ($p\bar{p}$ interaction points) are reconstructed from fits to tracks in each event and from the beam-line constraint, and the vertex with the highest total p_T of the associated tracks is chosen as the event vertex. In order to ensure that particles from the $p\bar{p}$ interactions are well measured by the CDF II detector, an event vertex is required to be within 60 cm of the center of the detector in z [10]. From the beam profile measured in data, the acceptance of the event z-vertex requirement has been determined to be 0.958 ± 0.002

The inclusive differential jet cross section can be defined as:

$$\frac{d^2\sigma}{dp_T dy} = \frac{1}{\Delta y}\frac{1}{\int \mathcal{L}dt}\frac{N_{\text{jet}}}{\Delta p_T}, \quad (3)$$

where N_{jet} is the number of jets in each p_T bin of width Δp_T, $\int \mathcal{L}dt$ is the effective integrated luminosity which accounts for trigger prescales, and Δy is the rapidity interval. The number of jets in each p_T bin is counted after jet energies are corrected on average as described below, and the differential cross sections are further corrected for the efficiencies of the $\not{E}_T/\sqrt{\sum E_T}$ and z-vertex cuts as well as the bin-to-bin jet migration effects due to finite energy measurement resolution as written in Sec. V C. The inclusive differential jet cross section is measured in five jet rapidity intervals, $|y| < 0.1$, $0.1 < |y| < 0.7$, $0.7 < |y| < 1.1$, $1.1 < |y| < 1.6$, and $1.6 < |y| < 2.1$ based on detector geometry.

V. JET ENERGY AND RESOLUTION CORRECTIONS

The jet energies measured by the calorimeters are affected by instrumental effects, such as calorimeter non-linearity and energy smearing due to finite energy resolution of the calorimeters. These biases are corrected for in several steps as outlined below. First, an η-dependent relative correction is applied in order to equalize in η the response of the calorimeters to jets. The equalized jet p_T is then corrected for the pileup effect, *i.e.,* the effect of additional $p\bar{p}$ interactions in the same bunch crossing. Then, a p_T-dependent absolute correction is applied to correct for the average under-measured hadron energy due to the non-linear response of the CDF calorimeters. These corrections are applied on a jet-by-jet basis and corrected jets are binned in p_T. This binned jet cross section is corrected for the efficiency of the event selection criteria and bin-to-bin jet migration effects due to energy smearing (unfolding). These corrections are derived by comparing the binned hadron-level cross section and the calorimeter-level cross sections corrected by the aforementioned jet-by-jet corrections using Monte Carlo events. After these corrections, the data have been corrected to the hadron level. In order to compare data with pQCD predictions, the effects of the underlying event (UE) and hadronization need to be accounted for, which is discussed in Sec. VII.

The Monte Carlo simulation used to derive the corrections, and the details of each correction step are described below.

A. Monte Carlo Simulation

The parton shower MC programs PYTHIA 6.2 [36] and HERWIG 6.5 [37] along with the CDF detector simulation are used to derive the various corrections which are applied to the data, and to estimate systematic uncertainties in the measurement. The proton and antiproton PDFs are taken from CTEQ5L [38]. PYTHIA Tune A [39], which refers to a set of parameters chosen to describe observables in the CDF data which are sensitive to the effects from the underlying event [40, 41], is used for all PYTHIA calculations mentioned in this paper. Tune A is

especially important for the UE correction discussed in Sec. VII.

The CDF II detector simulation is based on GEANT3 [42] in which a parametrized shower simulation, GFLASH [43], is used to simulate the energy deposited in the calorimeter. The GFLASH parameters are tuned to test-beam data for electrons and high-momentum charged pions and to the *in-situ* collision data for electrons from Z decays and low-momentum charged hadrons [44]. The MC simulation is used to derive various jet corrections to be applied to the data, and to evaluate the associated systematic uncertainties. However, the real calorimeter response to jets is not described perfectly by the calorimeter simulation. Differences in the relative jet energy response and jet energy resolution between the collision data and MC simulation events were investigated using p_T balance in dijet events [44] and the "bisector" method [45], respectively.

Comparisons of dijet p_T balance reveal that the variation of the jet energy scale with η is different for data and MC and that this difference depends on jet p_T at high rapidity ($|y| > 1.1$). For example, the jet energy scale in the plug calorimeter region is higher in MC than in data by $\sim 2\%$ and the difference increases slightly with jet p_T. This difference is accounted for by the relative corrections which are described in detail in Sec. V B 1.

The bisector method allows the jet energy resolution in the real CDF II detector and in the simulation to be compared. Events with a dijet topology are used for the study by requiring that only two jets have $p_T > 10$ GeV/c. In order to minimize the effects of pileup, only events with exactly one reconstructed primary vertex are used. Also, one jet is required to be in the central region of the detector ($0.1 < |y| < 0.7$) and is referred to as the "trigger" jet. The second jet is called the "probe" jet and can be in any other rapidity region ($|y| < 2.1$). A coordinate system is defined in the transverse plane with one axis aligned with the bisector of the two jets. With reference to Fig. 4, the following components related to the jet energy resolution are studied as functions of dijet mean p_T:

(a) $\sigma_\perp$ is the R.M.S. of the $\Delta p_{T\perp}$ distribution where $\Delta p_{T\perp} \equiv (p_{T_1} + p_{T_2})\cos(\Delta\phi_{12}/2)$: p_{T_1}, p_{T_2}, and $\Delta\phi_{12}$ refer to the p_T of the leading and next-to-leading jets and the azimuthal angle between the leading and next-to-leading jets, respectively. This component of the p_T imbalance is more sensitive to physics effects.

(b) $\sigma_{||}$ is the R.M.S. of the $\Delta p_{T_{||}}$ distribution where $\Delta p_{T_{||}} \equiv (p_{T_1} - p_{T_2})\sin(\Delta\phi_{12}/2)$. This component of the p_T imbalance is sensitive both to physics and detector effects.

(c) σ_D is the quadratic difference between $\sigma_{||}$ and $\sigma_\perp$ ($\sigma_D \equiv \sqrt{\sigma_{||}^2 - \sigma_\perp^2}$). This should be most sensitive to detector effects since the physics effects in $\sigma_\perp$,

which are expected to give an isotropic contribution in the transverse plane, are removed. It should also be noted that since both jets are contributing to σ_D, for a single jet $\sigma = \sigma_D/\sqrt{2}$.

For comparing the jet energy resolution in the real CDF II detector to that in the simulation, σ_D is used. In the rapidity region of $0.1 < |y| < 0.7$, the detector simulation reproduces the detector jet energy resolution accurately. Figure 5 shows $\sigma_\perp$, $\sigma_{||}$, and σ_D for data and PYTHIA events. The data to MC ratio of σ_D is used to compare the jet energy resolution in the real CDF II detector and in the simulation.

Figure 6 shows the result for the σ_D ratio in the other rapidity regions. In two rapidity regions ($0.7 < |y| < 1.1$ and $1.6 < |y| < 2.1$), it was found that MC slightly underestimates the jet energy resolution in data; to account for the differences, extra smearing is applied on jet energies in MC events to match the jet energy resolution between data and MC when the absolute and unfolding corrections are derived. The extra jet energy smearing results in $< 6\%$ changes in cross section in most bins, and $< 15\%$ in the most extreme cases.

B. Jet Corrections

1. Relative Correction

The calorimeter response to jets is not uniform in η. The non-uniformity arises from cracks between calorimeter modules and also from the different responses of the central and plug calorimeters. The relative correction is introduced to make the jet energy response flat in η.

The leading two jets in dijet events are expected to balance in p_T in the absence of QCD radiation. Therefore, p_T balance in dijet events is a useful tool to study the jet energy response as a function of η and to derive the relative correction. To determine the η-dependent relative jet energy correction, a jet with $0.2 < |\eta| < 0.6$ (where the CDF calorimeter is well understood) is defined as a trigger jet and the other jet is defined as a probe jet. The p_T balance ($\beta \equiv p_T^{\text{probe}}/p_T^{\text{trigger}}$) of these two jets [44] as a function of probe-jet η is shown in Fig. 7. It shows $\beta \sim 1$ in the region where the trigger jet is selected, *i.e.*, $0.2 < |\eta| < 0.6$. There are dips at $\eta \sim 0$ and ± 1 which are due to gaps between the calorimeter modules.

The η-dependent relative corrections are obtained from a fit to the β distribution at a given jet p_T. These corrections are derived independently for data and MC. The β ratio for data to MC simulation for all rapidity regions is shown in Fig. 8 as a function of jet p_T. A small additional p_T-independent correction is required in the region $|y| < 0.1$ to bring MC into agreement with data. As mentioned earlier, the data-MC difference in the relative jet energy scale depends on jet p_T at $|y| > 1.1$. Therefore an additional correction with p_T dependence is derived for the two highest $|y|$ regions and is applied in order to

match MC to data at any jet p_T. Due to lack of statistics at high p_T mainly in data, the uncertainty associated with this correction increases with increasing jet p_T as indicated by the dashed lines in Fig. 8.

2. Pileup Correction

Extra $p\bar{p}$ interactions in the same bunch crossing as the interaction which produced the jets can contribute energy to the jets. For the data sample used in this measurement, the average number of additional $p\bar{p}$ interactions per event is about two. The number of reconstructed primary vertices is a good estimator of the number of interactions in the same bunch crossing. The correction for the additional $p\bar{p}$ interactions is derived by measuring the average p_T in a randomly chosen cone as a function of the number of primary vertices in a sample of minimumbias events triggered only on a CLC coincidence between the two sides of the detector. The p_T in the randomly chosen cone scales linearly with the number of additional vertices in the event, and the pileup correction is derived from the slope of this line. For each additional vertex reconstructed in the event, 0.97 GeV/c is subtracted from the jet p_T.

3. Absolute Correction

As particles pass through the CDF calorimeter, not all of their energy is collected. The absolute correction is applied to each jet to compensate for this average energy loss. The correction is derived by comparing hadron-level and calorimeter-level jets using PYTHIA and the CDF detector simulation. Hadron-level and calorimeter-level jets are matched by their position in $y - \phi$ space ($\Delta R = \sqrt{(\Delta y)^2 + (\Delta \phi)^2} \leq 0.7$). In Fig. 9, the average hadron-level jet p_T is shown as a function of the calorimeter jet p_T in each rapidity region. These distributions are fit to a fourth-order polynomial and the fit is applied as a correction to the p_T of each jet in the data sample.

C. Unfolding Correction

The next step in correcting the jet p_T distribution to the hadron level is the unfolding correction, which accounts for smearing effects of the calorimeter and the efficiency of the event selection criteria. The hadron-level and calorimeter-level (after the jet corrections discussed above have been applied) cross sections from the PYTHIA MC events are compared on a bin-by-bin basis to derive the unfolding correction. Since these corrections depend on the jet p_T spectra, the PYTHIA events are reweighted to match the jet p_T spectra measured in data before the correction factors are calculated. These weights are derived by comparing the data corrected to

the hadron level to the PYTHIA prediction. The unfolding corrections shown in Fig. 10 are obtained from the weighted PYTHIA distributions and applied to the data. The change due to the reweighting of PYTHIA is small (less than 5%) except in the highest-p_T bins where the correction is still less than 20%. After the unfolding correction is applied to the data, the measurement has been corrected for all the instrumental effects and presented at the hadron level.

VI. SYSTEMATIC UNCERTAINTIES

The systematic uncertainties in the measurement are presented below.

Jet energy scale. The uncertainty in the jet energy scale mainly comes from the uncertainty in the tuning of the central calorimeter simulation based on the response to individual particles. This uncertainty is less than 3% of the jet energy over the entire jet energy range [44]. The resulting systematic uncertainty in the cross section measurement varies from 10% at low p_T up to 90% at high p_T in some rapidity regions. The fractional uncertainty on the jet cross section in the rapidity region $0.1 < |y| < 0.7$ due to the jet energy scale is shown in Fig. 11(a).

The jet energy scale uncertainty may be subdivided into a few components with different dependence on jet p_T [8]:

(1) A $\pm 1.8\%$ p_T-independent component which arises from the uncertainty in the calorimeter stability in time ($\pm 0.5\%$), uncertainty in the modeling of the jet fragmentation ($\pm 1.0\%$), uncertainty in the simulation of the electromagnetic calorimeter response($\pm 0.5\%$), and uncertainty in the simulation of the calorimeter response at the boundary between calorimeter towers ($\pm 1.3\%$) [44].

(2) Contributions due to the description of the calorimeter response to hadrons in three different momentum ranges [44]:

(2.a) $p < 12$ GeV/c

(2.b) $12 < p < 20$ GeV/c

(2.c) $p > 20$ GeV/c

These four components [(1), (2.a), (2.b), and (2.c)] are considered independent: Each of the four components is considered fully correlated in p_T and rapidity and is listed in Table II. This decomposition of the jet energy scale uncertainty for the region of $0.1 < |y| < 0.7$ is shown as a relative uncertainty on the jet cross section in Fig. 12.

Dijet p_T balance. The dependence on the dijet event selection definitions and statistical limitations yield a

0.5% uncertainty in the relative jet energy correction in all rapidity regions. In addition, at high p_T there is a p_T-dependent uncertainty on the correction in the higher rapidity regions ($|y| > 1.1$) due to low statistics. This uncertainty is considered correlated over p_T but uncorrelated across different rapidity regions. The fractional uncertainty on the cross section in the region of $0.1 < |y| < 0.7$ due to this dijet balance systematic uncertainty is shown in Fig. 11(c).

Pileup correction. The pileup correction is obtained from minimum-bias data, and the systematic uncertainty is determined so that it covers variations from a set of validation measurements. Measurements of the pileup correction from dijet, photon-jet, and $W \to e\nu$ events result in variations of less than 30% and this is taken as the size of the systematic uncertainty. This uncertainty results in less than 3% uncertainty in the cross section measurement. This uncertainty is considered fully correlated in p_T and rapidity. The fractional uncertainty on the cross section in the region of $0.1 < |y| < 0.7$ due to the pileup systematic uncertainty is shown in Fig. 11(e).

Unfolding and p_T-spectra. The difference between the PYTHIA and HERWIG predictions is taken as the systematic uncertainty on the unfolding correction, as they have different fragmentation models. The fractional uncertainty on the cross section in the region of $0.1 < |y| < 0.7$ due to the jet unfolding systematic uncertainty is shown in Fig. 11(d). This uncertainty is considered fully correlated in p_T and rapidity. As mentioned in Sec. V, PYTHIA events are reweighted when the unfolding corrections are determined so that the jet p_T spectrum agrees with what is observed in data. The uncertainty in the unfolding correction due to the dependence on the jet p_T spectra is taken conservatively from the change in the unfolding corrections with and without reweighting PYTHIA events. This reweighting is done independently in each rapidity region; therefore, the uncertainty is considered correlated over p_T but uncorrelated across different rapidity regions. The fractional uncertainty on the cross section in the rapidity region $0.1 < |y| < 0.7$ due to reweighting is shown in Fig. 11(f).

Jet energy resolution. Due to the sharply falling spectrum of the inclusive jet cross section, any imperfect modeling of the jet energy smearing in the detector simulation will affect the derived unfolding correction. The calorimeter-level jets in the PYTHIA events have been smeared by an extra amount such that σ_D as defined in the bisector method changes by 10%. The effect of this extra smearing on the jet differential cross section is taken as the systematic uncertainty due to resolution. The jet resolution

differences between data and MC events vary with rapidity and the corrections are performed independently in five rapidity regions; therefore, this uncertainty is considered correlated over p_T but uncorrelated across different rapidity regions. The fractional uncertainty on the cross section in the rapidity region $0.1 < |y| < 0.7$ due to the jet energy resolution is shown in Fig. 11(b).

Luminosity. There is a 6% uncertainty in normalization due to the luminosity measurement [30]. This uncertainty is considered fully correlated in p_T and rapidity.

The total systematic uncertainty on the hadron-level jet cross section for each jet rapidity region is shown in Fig. 13 [46]. The systematic uncertainties on the measured cross section from each source for each rapidity region are given in Tables III-VII.

VII.   THEORETICAL PREDICTIONS

Perturbative QCD calculations for the inclusive jet cross sections in hadron-hadron collisions have been performed so far only up to next-to-leading order, and their predictions are provided at the parton level [47–50] in which the final state is comprised of only two or three partons. Our measurement is compared with predictions from FASTNLO [51] which are based on the NLO-JET++ [49, 50] program. CTEQ6.1M [11] is used for the parton distribution functions (PDFs). The renormalization and factorization scales (μ_R and μ_F) are chosen to be the transverse momentum of the jet divided by two, which is the same as that used in the global QCD analyses [11, 17] to determine the PDFs. Using $\mu_R = \mu_F = p_T^{\text{jet}}$ gives up to 10% smaller predictions in the cross section. The uncertainties on the predictions due to PDF are estimated by using the 40 CTEQ6.1M error PDFs [11, 52], and the MRST2004 PDF [17] is also used to obtain a prediction. In order to account for the splitting and merging step of the Midpoint jet clustering algorithm when clustering partons after the parton shower or particles after hadronization [53], a parameter R_{sep} [54] with a value of 1.3 is used for the Midpoint algorithm at the NLO parton level. Two partons are clustered into a single jet if they are within R_{cone} of the jet centroid and within $R_{\text{cone}} \times R_{\text{sep}}$ of each other. An R_{sep} value of 2.0 (*i.e.,* the Midpoint algorithm without R_{sep}) yields $< 5\%$ larger cross sections for NLO pQCD predictions.

As mentioned earlier, NLO pQCD calculations provide predictions not at the hadron level, to which the data are corrected, but at the parton level, *i.e.,* they do not account for the underlying event and hadronization effects. In order to compare the data corrected to the hadron level with predictions for jets clustered from partons as obtained from NLO pQCD calculations, such effects must be accounted for. The underlying event contributes energy to the jet cone that is not associated with the hard

scattering event, *i.e.*, energy from collisions of other partons in the proton and antiproton. Hadronization may cause particles originating from partons whose trajectories lie inside the jet cone to go outside of the jet cone. The effect of hard gluon emission outside the jet cone is already accounted for in NLO pQCD predictions, and thus it is not included in the corrections discussed below.

The bin-by-bin parton-to-hadron-level ($C_{p \to h}$) corrections are obtained by applying the Midpoint clustering algorithm to the hadron-level and to the parton-level outputs of the PYTHIA Tune A dijet Monte Carlo samples, generated with and without an underlying event. The samples without the underlying event were generated by turning off multiple parton interactions (MPIs). The parton-to-hadron-level correction increases the NLO pQCD cross section predictions by about 10% at low p_T and is negligible at high p_T as shown in Fig. 14.

The uncertainty on the parton-to-hadron-level correction is estimated from the difference in the predictions for this correction from HERWIG and PYTHIA. HERWIG does not include MPIs in its underlying event model, and instead relies on initial state radiation (ISR) and beam remnants to populate the underlying event. The difference between HERWIG and PYTHIA is conservatively taken for this systematic uncertainty, and this uncertainty is represented by the shaded bands in Fig. 14.

VIII. RESULTS

The measured inclusive differential jet cross sections at the hadron level are shown in Fig. 15, and Tables VIII-XII show the lists of the measured cross sections for each jet p_T and rapidity bin together with the statistical and total systematic uncertainties, and parton-to-hadron-level correction factors. The ratios of the measured cross sections to the NLO pQCD predictions from FASTNLO (corrected to the hadron level) based on the CTEQ6.1M PDF are shown in Fig. 16 together with the theoretical uncertainties due to PDF. The measured inclusive jet cross sections tend to be lower but still in agreement with the NLO pQCD predictions within the experimental and theoretical uncertainties.

To quantify the comparisons, a procedure based on the χ^2 defined as:

$$\chi^2 = \sum_{i=1}^{\mathrm{nbin}} \frac{[\sigma_i^{\mathrm{data}} - \sigma_i^{\mathrm{theory}}]^2}{[(\delta\sigma_i^{\mathrm{data-stat}})^2 + (\delta\sigma_i^{\mathrm{theory-stat}})^2]} + \sum_{j=1}^{\mathrm{nsyst}} s_j^2, \tag{4}$$

$$\sigma_i^{\mathrm{theory}} = \sigma_{i,0}^{\mathrm{theory}} + \sum_{j=1}^{\mathrm{nsyst}} s_j \times \delta\sigma_{i,j}^{\mathrm{syst}} \tag{5}$$

is used where σ_i^{data} and $\delta\sigma_i^{\mathrm{data-stat}}$ are the measured cross section and its statistical uncertainty in the i-th data point, and $\sigma_i^{\mathrm{theory}}$ and $\sigma_i^{\mathrm{theory-stat}}$ are the corresponding theoretical prediction and its statistical uncertainty. The $\sigma_i^{\mathrm{theory}}$ may be shifted from the nominal

theoretical prediction for the i-th data point, $\sigma_{i,0}^{\mathrm{theory}}$, as shown in Eq. (5), where $\delta\sigma_{i,j}^{\mathrm{syst}}$ is the systematic uncertainty in the i-th data point due to the j-th systematic uncertainty and s_j is the standard deviation in the j-th systematic uncertainty. The first sum in Eq. (4) is carried out over all data points, and the second sum in Eq. (4) and the sum in Eq. (5) are over all independent sources of the systematic uncertainties. These systematic shifts s_j are chosen to minimize the χ^2 defined above using the MINUIT program [55]. This χ^2 definition is basically the same as those used in the previous CDF inclusive jet cross section measurements [8, 31], and this χ^2 is equivalent to the one calculated using the covariance matrix technique.

In the χ^2 calculation, the systematic uncertainties due to jet energy scale (four independent contributions), luminosity, pileup, and unfolding are treated as correlated across all data points in p_T and rapidity. The uncertainties from dijet p_T balance, jet energy resolution, and p_T spectra are treated as correlated over p_T in a rapidity region but are uncorrelated across different rapidity regions, as discussed in Sec. VI. As for the theoretical uncertainty, the uncertainty on $C_{p \to h}$ is considered as fully correlated across all data points, however the PDF and scale uncertainties are not considered. This χ^2 test yields the probabilities of 71, 91, 23, 69 and 91% when it is performed separately in the five rapidity regions of $|y| < 0.1$, $0.1 < |y| < 0.7$, $0.7 < |y| < 1.1$, $1.1 < |y| < 1.6$, and $1.6 < |y| < 2.1$. The global χ^2 test which is performed simultaneously on all the data points in all five rapidity regions yields the reduced χ^2, $\chi^2/\mathrm{n.d.f.} = 94/72$ corresponding to a probability of 4%.

As shown in Fig. 16, the experimental uncertainties in the measurement are comparable or somewhat smaller than the PDF uncertainties on the theoretical predictions, especially in higher $|y|$ regions, and thus this measurement will lead to useful constraints on PDFs when it is included in QCD global fits.

While this measurement was underway, a new cone-based jet clustering algorithm, called SISCone [56], was proposed which is a seedless algorithm and thus infrared safe to all orders in pQCD. We have studied the impact of using the SISCone algorithm instead of the Midpoint algorithm in Appendix A and found that the ratio of the measured cross section over theoretical predictions would change by only ~1%. Therefore, both algorithms will yield similar data-theory comparisons and lead to a similar PDF parametrization when the measurement is included in QCD global fits.

IX. COMPARISON WITH THE MEASUREMENT USING k_T CLUSTERING ALGORITHM

As mentioned in Sec. I, the CDF collaboration has recently made a measurement of the inclusive jet cross section using the k_T jet clustering algorithm [8]. In this

section, our measurement is compared with the results obtained with the k_T algorithm with $D = 0.7$ by taking the ratio of the cross sections from the two measurements and comparing it with theoretical predictions. In order to make a useful comparison, the correlations between the statistical and systematic uncertainties were studied and are presented below.

A. Statistical Correlation

The datasets used in the two measurements have about 90% overlap, and even in the same events the Midpoint and k_T algorithms may lead to a different set of jets and thus populate different p_T bins which are treated as statistically independent. In order to study the statistical correlation between the two measurements, both k_T and Midpoint jet clustering algorithms are applied in events used in both measurements and if the resulting jets from both algorithms are matched in $y - \phi$ space within $R < 0.7$ and fall into the same jet p_T and rapidity bin, those jets are treated as correlated, otherwise they are considered uncorrelated. This was done for the data points for which events from the jet100 and jet70 triggers are used. The situation is more complicated for data points from jet20 and jet50 triggers where prescale factors were changed during the data taking period. Thus, the statistical uncertainties are treated as uncorrelated in the two measurements for data points for which the jet20 and jet50 trigger events are used. It should be noted that the statistics are high in these triggers and the statistical uncertainties are small compared with the systematic uncertainties.

B. Systematic Correlation

The systematic uncertainties arising from the jet energy scale, unfolding correction, and underlying event modeling were determined with the same methods in the two measurements, and thus these uncertainties are treated as fully correlated between the two measurements, *i.e.*, the systematic uncertainties are canceled in the ratio of the two measurements.

In this analysis, the pileup correction is determined by measuring the average p_T in a randomly chosen cone as a function of the number of primary vertices in minimumbias data as discussed in Sec. V. However, a different method is used in the measurement using the k_T algorithm [8], and thus uncertainties arising from pileup corrections are treated as uncorrelated. The details of η-dependent jet corrections are also compared and it is concluded that this uncertainty is also uncorrelated.

The correction for the jet p_T resolution and the associated systematic uncertainties between the two measurements are determined in a similar way in the two measurements but the size of the correction was found to be different. The jet p_T resolution difference between

data and MC events is measured in dijet events with third-jet p_T <10 GeV/c in order to use dijet events with a clear back-to-back structure, and this dijet event selection is not equivalent when jets are clustered by the k_T algorithm and by the Midpoint algorithm. In addition, the jet resolution correction is sensitive to the procedure of applying the η-dependent relative jet correction. By varying the dijet selection requirement and the η-dependent jet correction procedure, 35% of the size of the jet p_T resolution uncertainty is found to be uncorrelated between the two measurements.

C. Results

The ratio of the cross section measured with the k_T algorithm to that with the Midpoint algorithm is shown in Fig. 17. This ratio of the NLO pQCD predictions as given by FASTNLO (corrected to the hadron level) and the ratio from PYTHIA are also included. It should be noted that the rapidity region where the agreement is only marginal $(0.7 < |y| < 1.1)$ corresponds to the crack between the central and plug calorimeters. In the other regions, good agreement is observed over a large range of rapidity and p_T. This agreement means that both algorithms observe similar systematic trends when compared to NLO pQCD predictions and favor the same PDF parametrization. In addition, the agreement between the data, PYTHIA, and NLO pQCD predictions for these ratios provide strong evidence that these clustering algorithms are behaving in a consistent way when clustering particles at the parton, hadron, and calorimeter-tower (detector) levels.

X. CONCLUSIONS

A measurement has been presented of the inclusive jet cross section for jets clustered by the Midpoint jet-finding algorithm using 1.13 fb^{-1} of data collected by the CDF experiment. The measured cross sections tend to be lower than the central NLO pQCD predictions, but they are still consistent when systematic uncertainties are taken into account. Similar trends are also observed in the recent results from CDF using the k_T algorithm [8] and from D0 using the Midpoint algorithm [9]. In the forward regions, the measurement precision is better than current PDF uncertainties. When included in QCD global fits this will provide further constraints on PDFs, especially the gluon distributions at high x. Since the measured cross sections tend to be lower than the central NLO pQCD predictions, the inclusion of this measurement to QCD global fits will lead to somewhat reduced gluon densities at high x. The results are also compared to the recent measurement of the inclusive jet cross section using the k_T jet clustering algorithm [8], and it is found that the ratios of the cross sections measured with the two algorithms are in reasonable agreement with theoretical expectations.

APPENDIX A: SEEDLESS INFRARED-SAFE CONE ALGORITHM

Recently, a cone algorithm (SISCone) has been proposed which is a seedless algorithm and thus infrared safe to all orders in pQCD [56]. One of the main problems with the use of a seedless cone algorithm has been its slow speed with respect to the seeded cone algorithms (such as the Midpoint algorithm); however, the SISCone algorithm has a speed comparable to the seeded cone algorithms. We have studied the differences in the inclusive jet cross section between the Midpoint algorithm used in this paper and the SISCone algorithm using PYTHIA Monte Carlo samples. Studies with the PYTHIA samples generated with the Tune A parameters show that, at the hadron level, the SISCone algorithm yields the inclusive jet cross section lower than the Midpoint algorithm by $\sim 5\%$ at low p_T and $\sim 2\%$ in the highest p_T bins independent of jet rapidities; however, the PYTHIA samples generated without multiple parton interactions show that the parton-level inclusive jet cross section is consistent between the Midpoint algorithm and SISCone algorithm to better than 1%, if the same cone radius and the same merging fraction f_{merge} are used for both algorithms [13]. Therefore, although the inclusive jet cross section measured at the hadron level will decrease by up to $\sim 5\%$ with the SISCone algorithm, the change will be compensated by the parton-to-hadron-level corrections applied to the NLO pQCD predictions, and thus, the comparisons between the measured cross section and NLO pQCD predictions will essentially be the same.

[1] E. Eichten, K. D. Lane, and M. E. Peskin, Phys. Rev. Lett. **50**, 811 (1983).

[2] K. Lane, arXiv:hep-ph/9605257.

[3] D. J. Gross and F. Wilczek, Phys. Rev. D **8**, 3633 (1973).

[4] H. Fritzsch, M. Gell-Mann, and H. Leutwyler, Phys. Lett. B **47**, 365 (1973).

[5] R. K. Ellis, W. J. Stirling and B. R. Webber, Camb. Monogr. Part. Phys. Nucl. Phys. Cosmol. **8**, 1 (1996).

[6] A. Abulencia *et al.* (CDF Collaboration), Phys. Rev. D **74**, 071103 (2006).

[7] A. Abulencia *et al.* (CDF Collaboration), Phys. Rev. Lett. **96**, 122001 (2006).

[8] A. Abulencia *et al.* (CDF Collaboration), Phys. Rev. D **75**, 092006 (2007).

[9] V. M. Abazov *et al.* (D0 Collaboration), Phys. Rev. Lett. **101**, 062001 (2008).

[10] We use a cylindrical coordinate system with the z coordinate along the proton beam direction and the origin at the center of the detector, the azimuthal angle ϕ, and the polar angle θ usually expressed through the pseudorapidity $\eta = -\ln\tan(\theta/2)$. The rapidity y is defined as $y = 1/2\ln((E + p_z)/(E - p_z))$ where E denotes the energy and p_z is the momentum component along z. The transverse energy and transverse momentum are given by $E_T = E\sin(\theta)$ and $p_T = p\sin(\theta)$ where p is the magnitude of the momentum vector.

[11] D. Stump *et al.*, J. High Energy Phys. 10 (2003) 046.

[12] G. C. Blazey *et al.*, arXiv:hep-ex/0005012.

[13] S. D. Ellis *et al.*, Prog. Part. Nucl. Phys. **60**, 484 (2008).

[14] C. Buttar *et al.*, arXiv:0803.0678.

[15] M. G. Albrow *et al.*, arXiv:hep-ph/0610012.

[16] In the previous CDF measurement [6], an additional step called the "Search Cone" was included in the Midpoint algorithm. This step is removed in this measurement as recommended by the TeV4LHC QCD Working Group. For further discussions, see Ref. [15].

[17] A. D. Martin, R. G. Roberts, W. J. Stirling, and R. S. Thorne, Phys. Lett. B **604**, 61 (2004).

[18] S. D. Ellis and D. E. Soper, Phys. Rev. D **48**, 3160 (1993).

[19] B. Abbott *et al.* (D0 Collaboration), Phys. Rev. Lett. **82**, 2451 (1999).

[20] B. Abbott *et al.* (D0 Collaboration), Phys. Lett. B **525**, 221 (2002).

[21] D. Acosta *et al.* (CDF Collaboration), Phys. Rev. D **71**, 052003 (2005).

[22] A. Sill, Nucl. Instrum. Methods Phys. Res., Sect. A **447**, 1 (2000).

[23] T. Affolder *et al.*, Nucl. Instrum. Methods Phys. Res., Sect. A **453**, 84 (2000).

[24] T. Affolder *et al.*, Nucl. Instrum. Methods Phys. Res., Sect. A **526**, 249 (2004).

[25] L. Balka *et al.*, Nucl. Instrum. Methods Phys. Res., Sect. A **267**, 272 (1988).

[26] S. R. Hahn *et al.*, Nucl. Instr. Methods Phys. Res. A **267**, 351 (1988).

[27] S. Bertolucci *et al.*, Nucl. Instrum. Methods Phys. Res., Sect. A **267**, 301 (1988).

[28] R. Oishi, Nucl. Instrum. Methods Phys. Res., Sect. A

453, 227 (2000).

[29] M. Albrow *et al.*, Nucl. Instrum. Methods Phys. Res., Sect. A **480**, 524 (2002).

[30] D. Acosta *et al.*, Nucl. Instrum. Methods Phys. Res., Sect. A **494**, 57 (2002).

[31] T. Affolder *et al.* (CDF Collaboration), Phys. Rev. D **64**, 032001 (2001).

[32] W. B. Kilgore and W. T. Giele, Phys. Rev. **D55**, 7183 (1997).

[33] The hadron level in the Monte Carlo generators is defined using all final state particles with lifetime above 10^{-11}s.

[34] p_T^{JET} refers to the transverse momentum of jets after the absolute jet energy correction has been made while p_T^{CAL} refers to uncorrected jet p_T.

[35] The missing transverse energy ($\not{E}_T$) is defined by $\not{E}_T = |\vec{\not{E}}_T|$, $\vec{\not{E}}_T = -\sum_i E_T^i \hat{\mathbf{n}}_{\mathbf{i}}$, where $\hat{\mathbf{n}}_{\mathbf{i}}$ is a unit vector perpendicular to the beam axis and pointing at the ith calorimeter tower. The sum is over all the calorimeter towers with $E_T > 100$ MeV and $|\eta| < 3.6$. We define the missing E_T significance as $\not{E}_T/\sqrt{\sum E_T} = |\vec{\not{E}}_T|/\sqrt{\sum_i E_T^i}$.

[36] T. Sjostrand *et al.*, Comput. Phys. Commun. **135**, 238 (2001).

[37] G. Corcella *et al.*, J. High Energy Phys. 01 (2001) 010.

[38] H. L. Lai *et al.* (CTEQ Collaboration), Eur. Phys. J. C **12**, 375 (2000).

[39] R. Field, presented at *Fermilab ME/MC Tuning Workshop*, Fermilab, October 4, 2002. PYTHIA Tune A implies that the following parameters are set in PYTHIA with CTEQ5L: PARP(67)=4, MSTP(82)=4, PARP(82)=2, PARP(84)=0.4, PARP(85)=0.9, PARP(86)=0.95, PARP(89)=1800, PARP(90)=0.25.

[40] T. Affolder *et al.* (CDF Collaboration), Phys. Rev. D **65**, 092002 (2002).

[41] R. Field and R. C. Group (CDF Collaboration), arXiv:hep-ph/0510198.

[42] R. Brun, F. Bruyant, M. Maire, A. C. McPherson, and P. Zanarini (1987), cern-DD/EE/84-1.

[43] G. Grindhammer, M. Rudowicz, and S. Peters, Nucl. Instrum. Methods Phys. Res., Sect. A **290**, 469 (1990).

[44] A. Bhatti *et al.*, Nucl. Instrum. Methods Phys. Res., Sect. A **566**, 375 (2006).

[45] P. Bagnaia *et al.* (UA2 Collaboration), Phys. Lett. B **144**, 283 (1984).

[46] The 6% uncertainty on the luminosity is not included.

[47] S. D. Ellis, Z. Kunszt, and D. E. Soper, Phys. Rev. Lett. **64**, 2121 (1990).

[48] W. T. Giele, E. W. N. Glover, and D. A. Kosower, Nucl. Phys. **B403**, 633 (1993).

[49] Z. Nagy, Phys. Rev. D **68**, 094002 (2003).

[50] S. Catani and M. H. Seymour, Nucl. Phys. **B485**, 291 (1997).

[51] T. Kluge, K. Rabbertz, and M. Wobisch, arXiv:hep-ph/0609285.

[52] J. Pumplin *et al.*, Phys. Rev. D **65**, 014013 (2002).

[53] S. D. Ellis, J. Huston, and M. Tonnesmann, eConf C010630, P513 (2001).

[54] S. D. Ellis and D. E. Soper, Phys. Rev. D **48**, 3160 (1993).

[55] F. James and M. Roos, Comput. Phys. Commun. **10**, 343 (1975).

[56] G. P. Salam and G. Soyez, J. High Energy Phys. 05 (2007) 086.
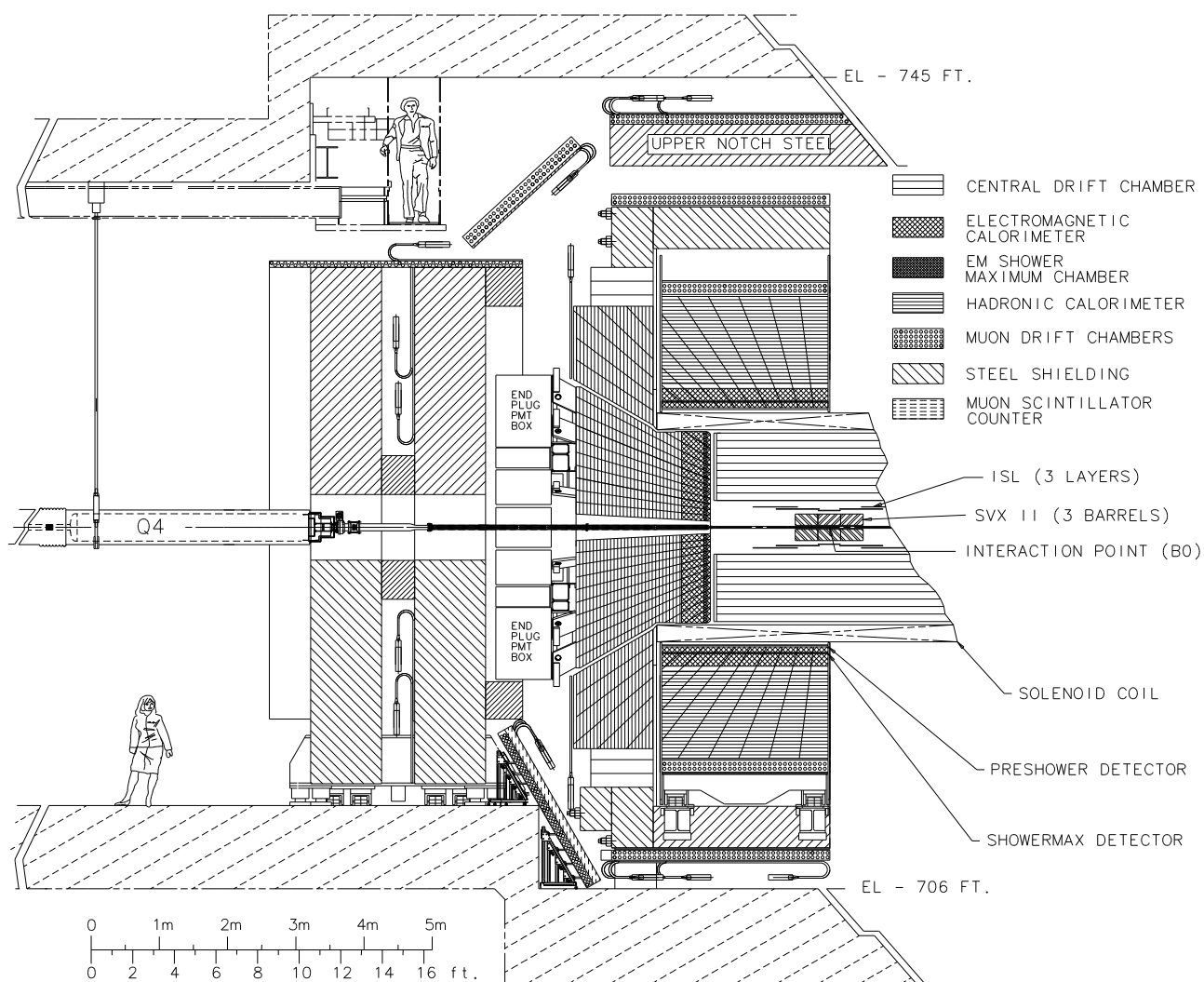
FIG. 1: Elevation view of half of the CDF Run II detector.
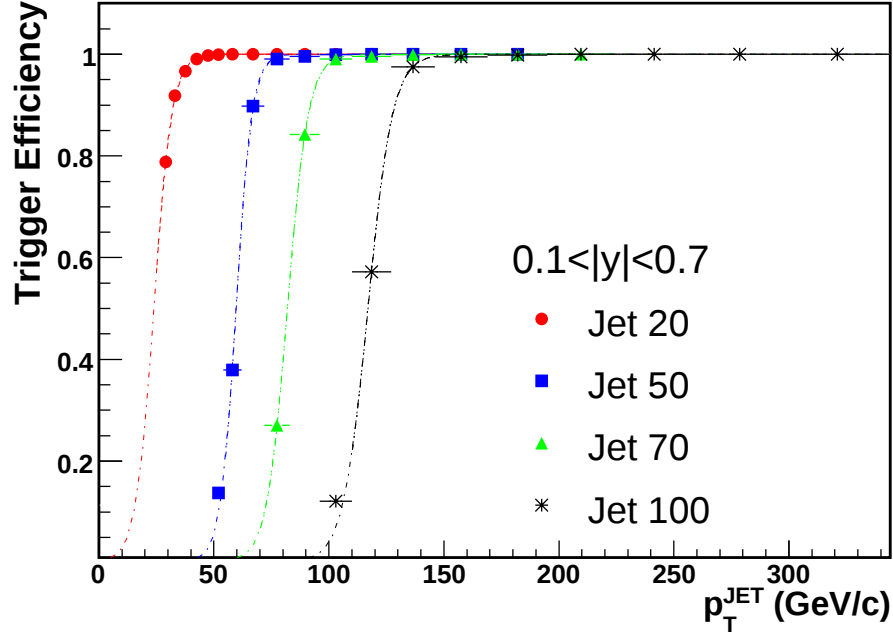
FIG. 2: Jet trigger efficiencies as functions of jet p_T for four trigger paths in the rapidity region $0.1 < |y| < 0.7$. The jet p_T measured by the calorimeters is corrected as described in Sec. V in these distributions.
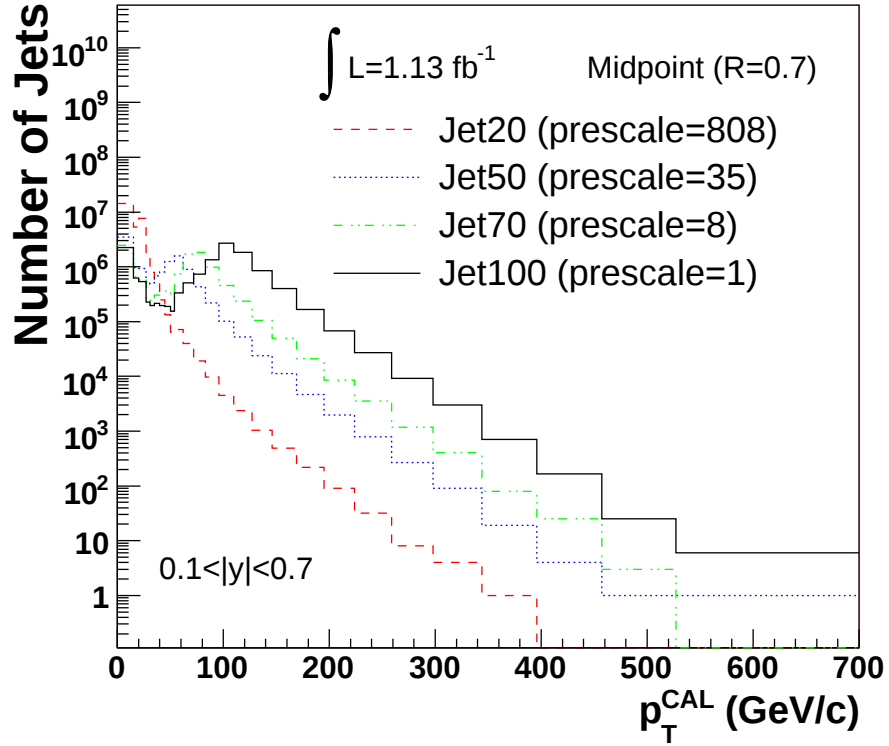
FIG. 3: Jet yield distributions as functions of jet p_T for four trigger paths in the rapidity region $0.1 < |y| < 0.7$ with no correction for trigger prescales.
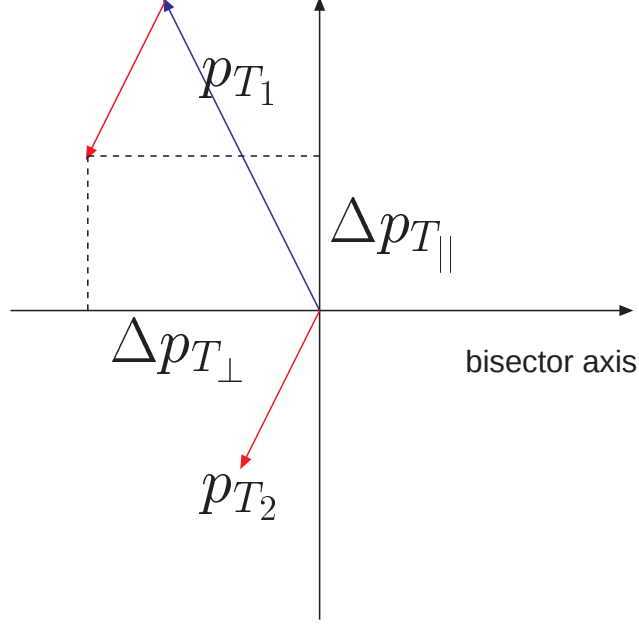
FIG. 4: The bisector variables described in the text are labeled in the diagram of the transverse plane shown above. $\Delta p_{T_\perp}$ ($\Delta p_{T_\parallel}$) is defined to be the component along (perpendicular to) the bisector axis of the sum of the jet p_Ts.
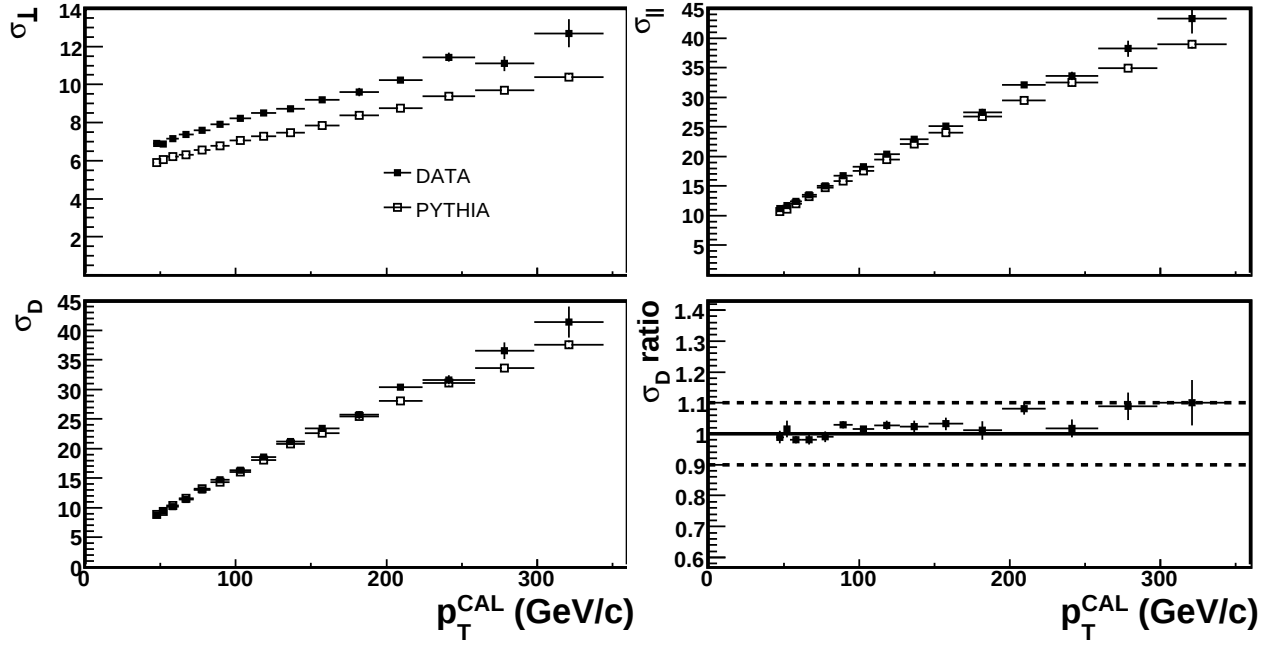
FIG. 5: The $\sigma_\perp$, $\sigma_\parallel$, and σ_D distributions as functions of jet p_T in data and PYTHIA MC events in the region of $0.1 < |y| < 0.7$. The data/PYTHIA ratio of σ_D is also shown.
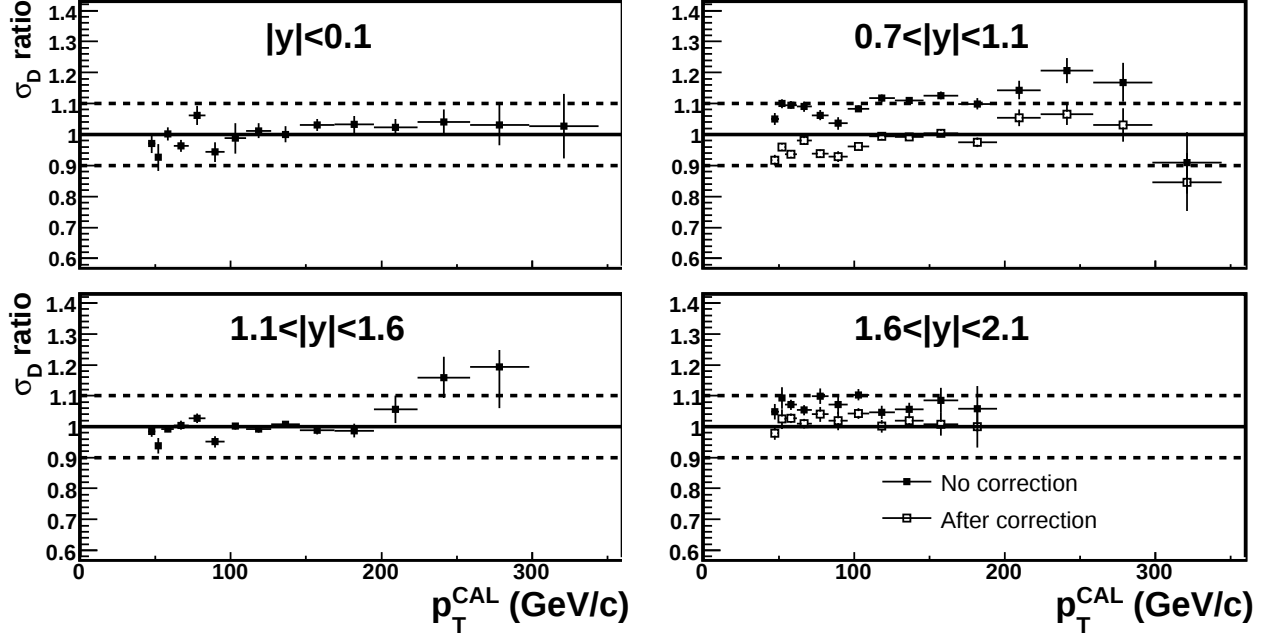
FIG. 6: The data/MC ratio in σ_D in four rapidity regions, $|y| < 0.1$, $0.7 < |y| < 1.1$, $1.1 < |y| < 1.6$, and $1.6 < |y| < 2.1$ (solid squares). The same distribution in the region of $0.1 < |y| < 0.7$ is shown in Fig. 5. In the two regions where the simulation slightly underestimates the detector resolution, the MC is smeared by an additional amount to bring simulation and data into agreement (open squares).
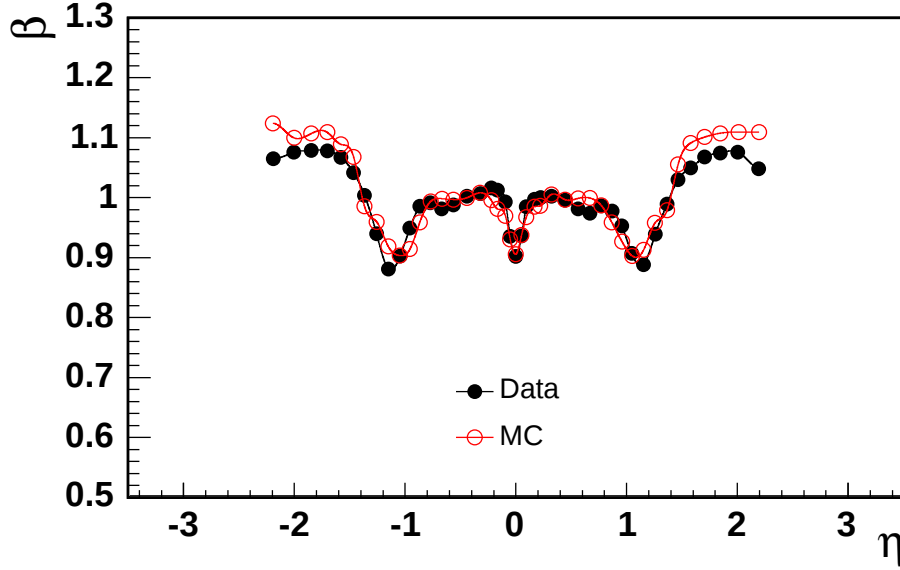
FIG. 7: The dijet p_T balance (β), as defined in Sec. V B 1, for data and PYTHIA MC events as a function of jet η.
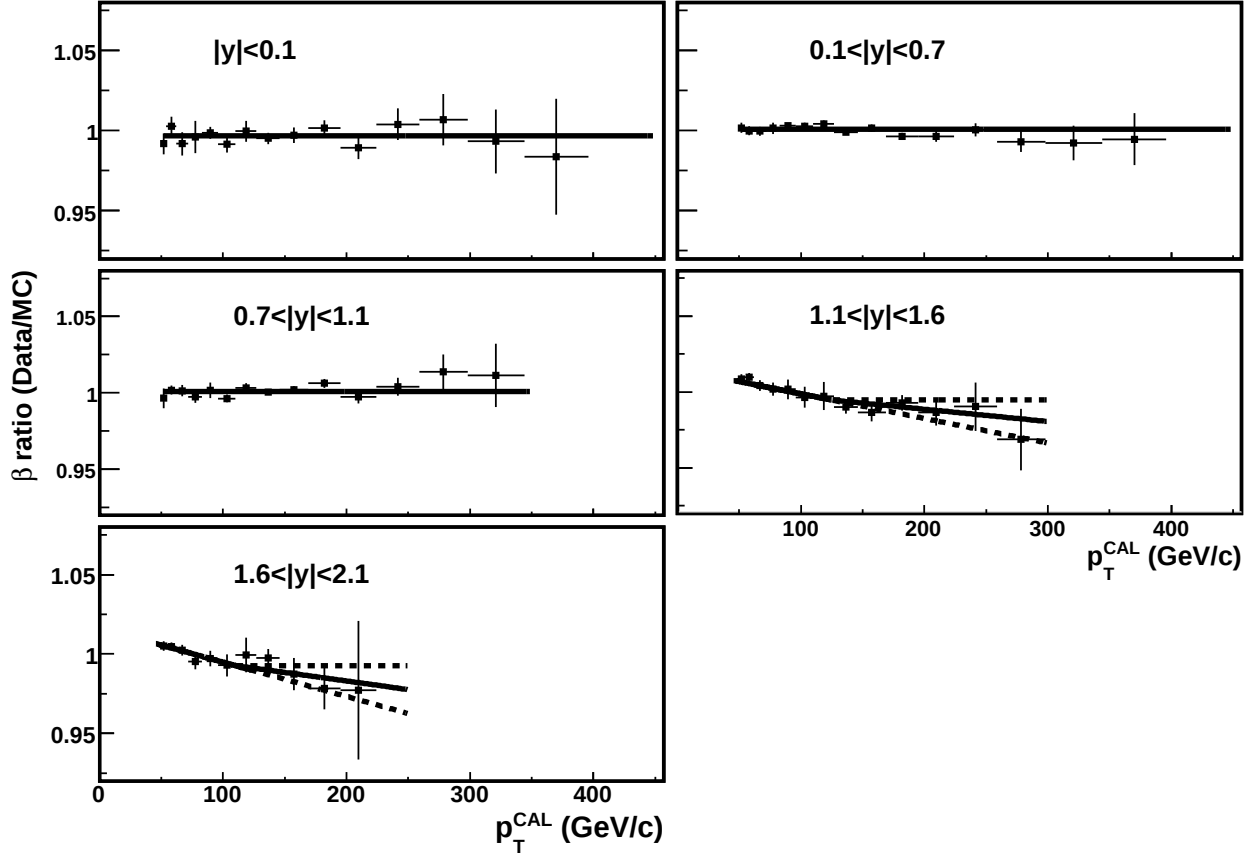
FIG. 8: The data/MC ratio in dijet p_T balance (β) in five rapidity regions after the p_T-independent relative correction have been applied. An additional correction is applied to the MC events to bring them into agreement with data in the regions of $|y| < 0.1$, $1.1 < |y| < 1.6$, and $1.6 < |y| < 2.1$. In the most forward regions ($1.1 < |y| < 1.6$ and $1.6 < |y| < 2.1$), an additional systematic uncertainty is quoted due to the limited statistics at large p_T which is shown by the the dashed lines.
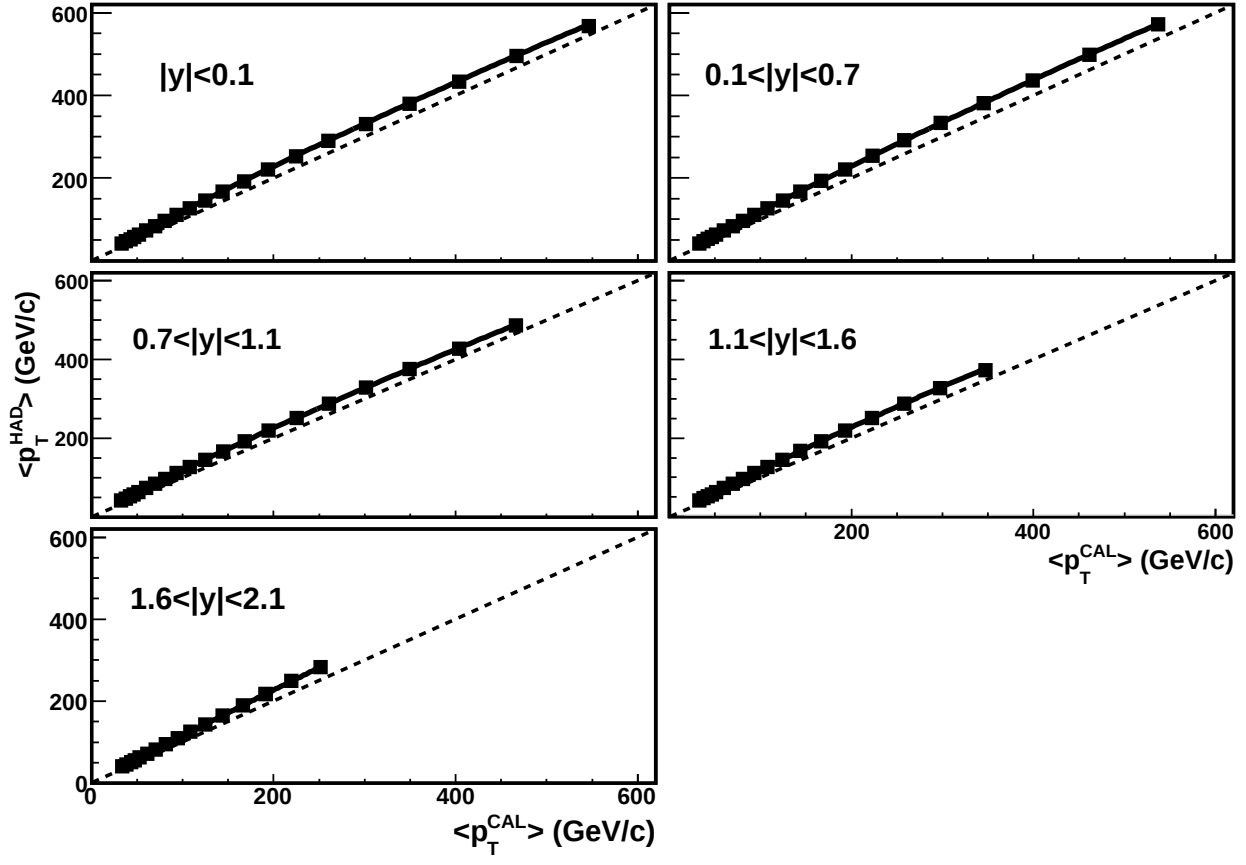
FIG. 9: The average hadron level jet p_T as a function of the average calorimeter jet p_T in five rapidity regions. The dashed lines correspond to $\langle p_T^{\mathrm{CAL}} \rangle = \langle p_T^{\mathrm{HAD}} \rangle$.
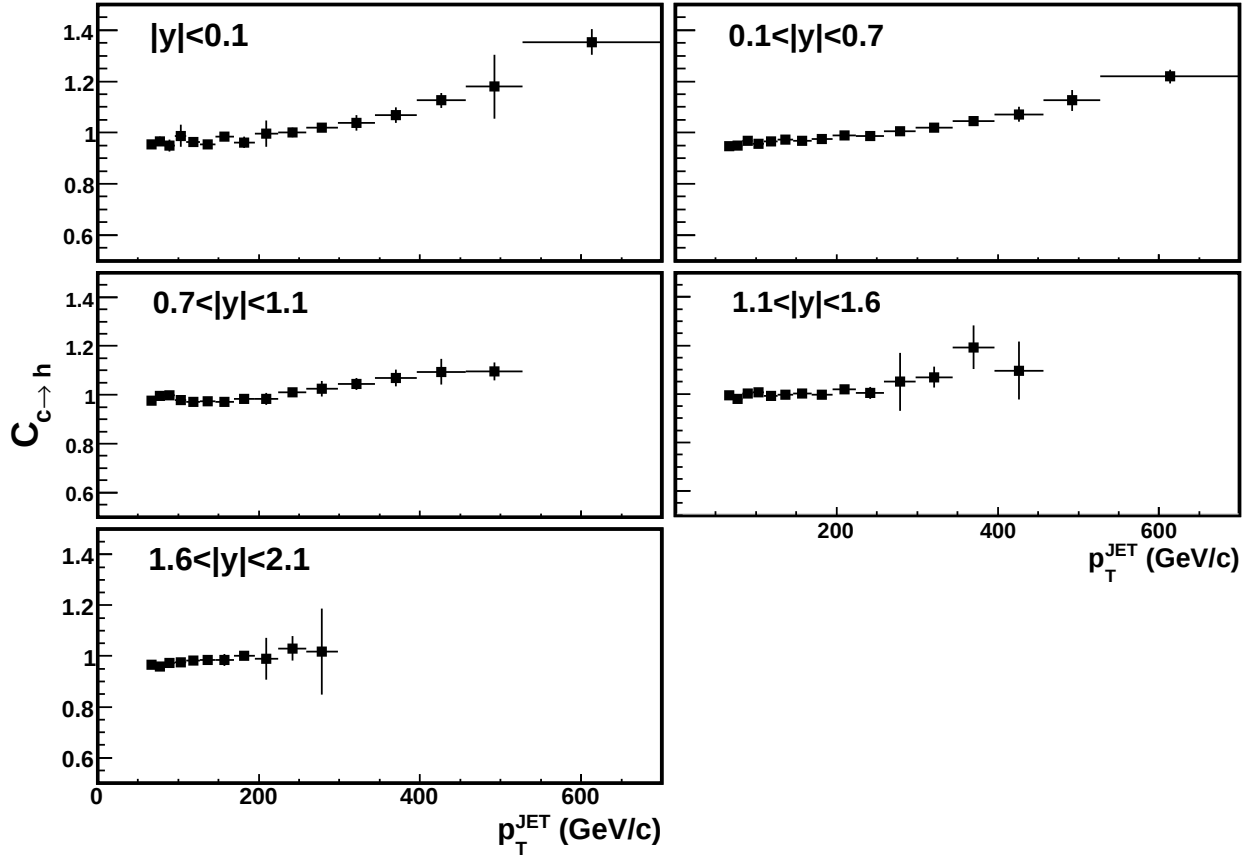
FIG. 10: The unfolding correction factors as functions of jet p_T in five rapidity regions.
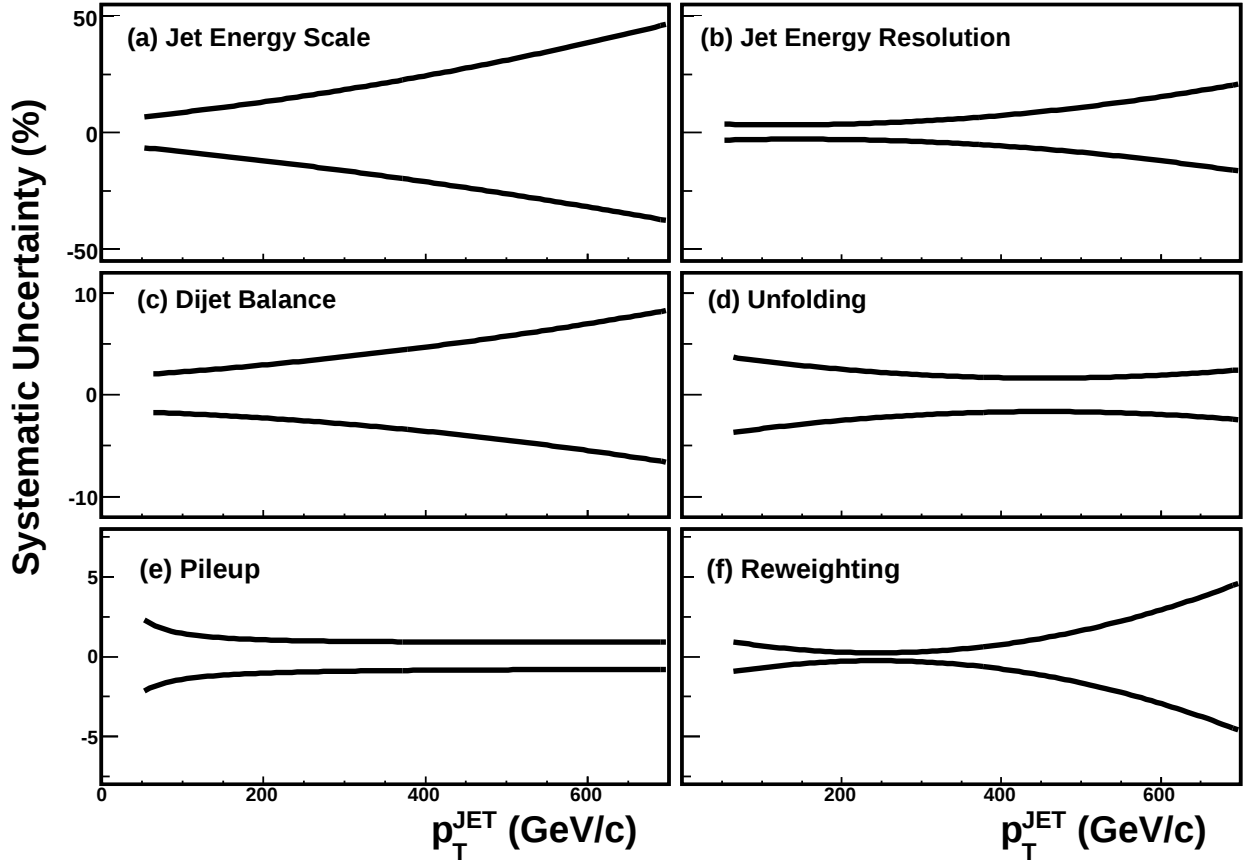
FIG. 11: The systematic uncertainty on the cross section in the rapidity region $0.1 < |y| < 0.7$ for each source considered in the measurement.
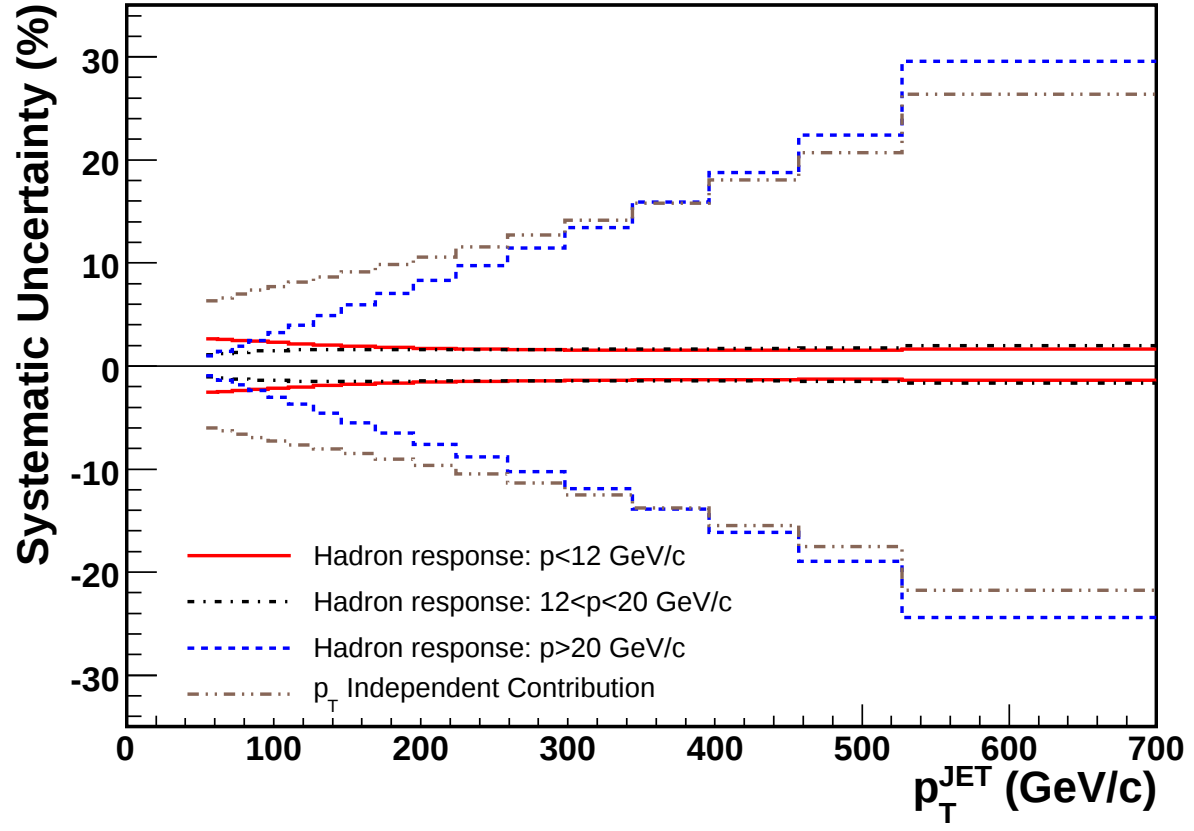
FIG. 12: The relative uncertainty on the jet cross section in the rapidity region $0.1 < |y| < 0.7$ due to different components of the jet energy scale systematic uncertainties. The decomposition includes contributions due to the description of the calorimeter response to hadrons for three different ranges of hadron momentum and a p_T-independent component as discussed in Sec. VI.
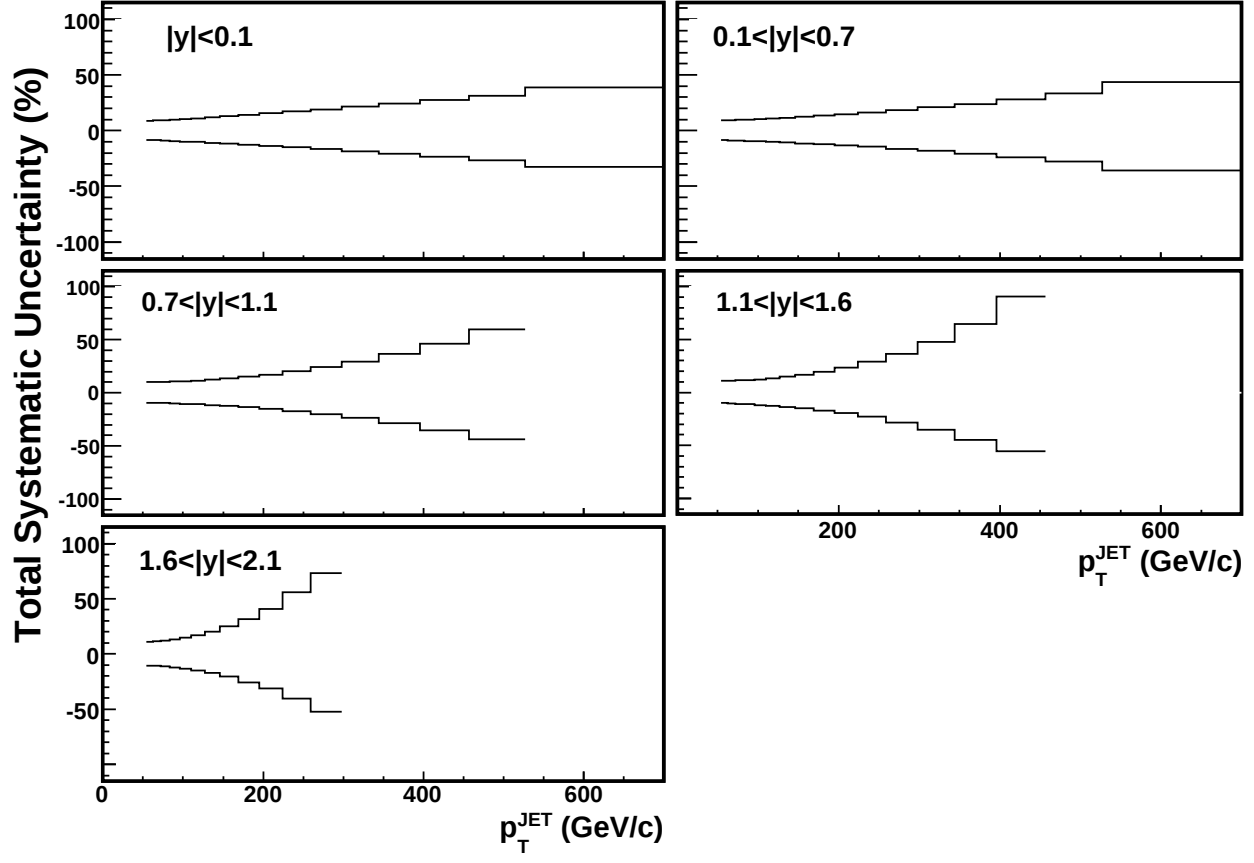
FIG. 13: The total systematic uncertainty on the cross section in five rapidity regions.
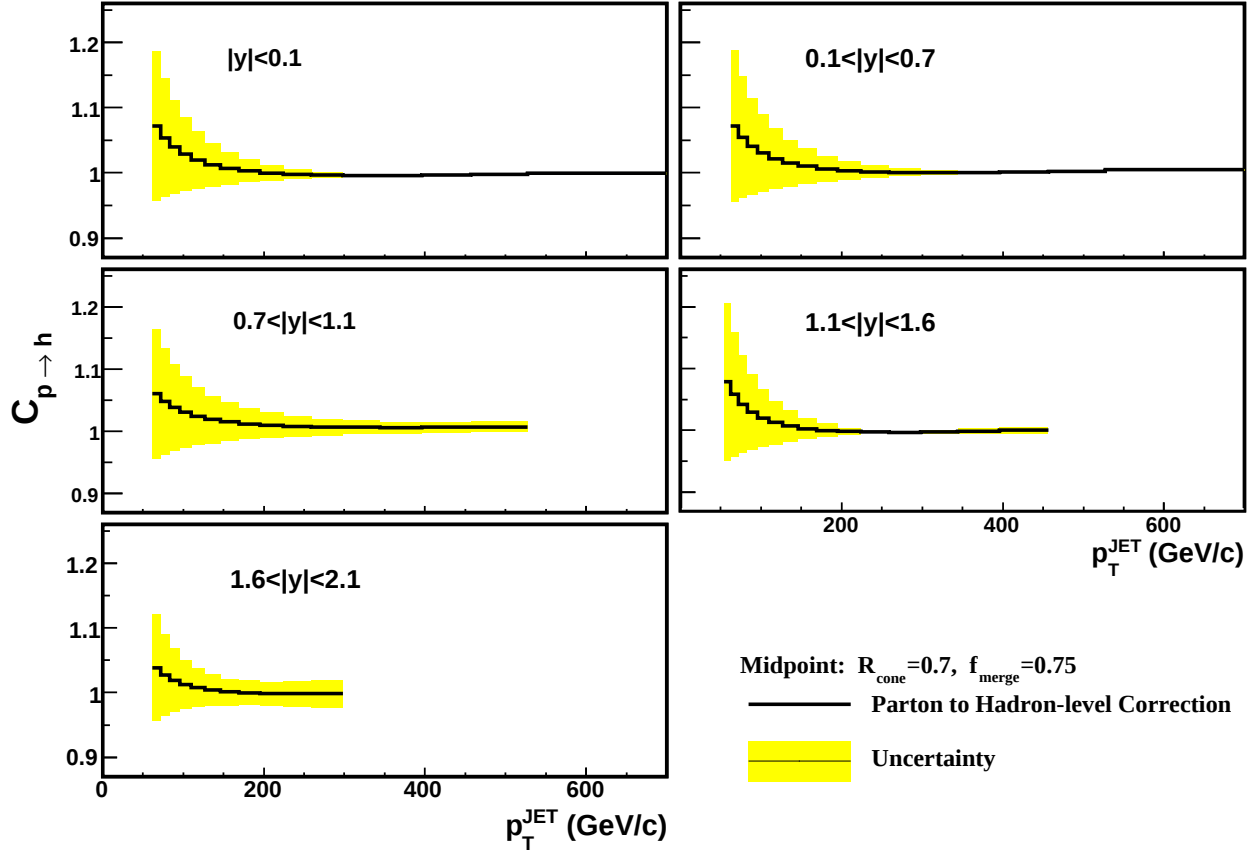
FIG. 14: The parton-to-hadron-level correction for five rapidity regions. The correction is derived from PYTHIA (solid line) and the difference between the HERWIG and PYTHIA prediction for the correction is conservatively taken as the systematic uncertainty (shaded bands).
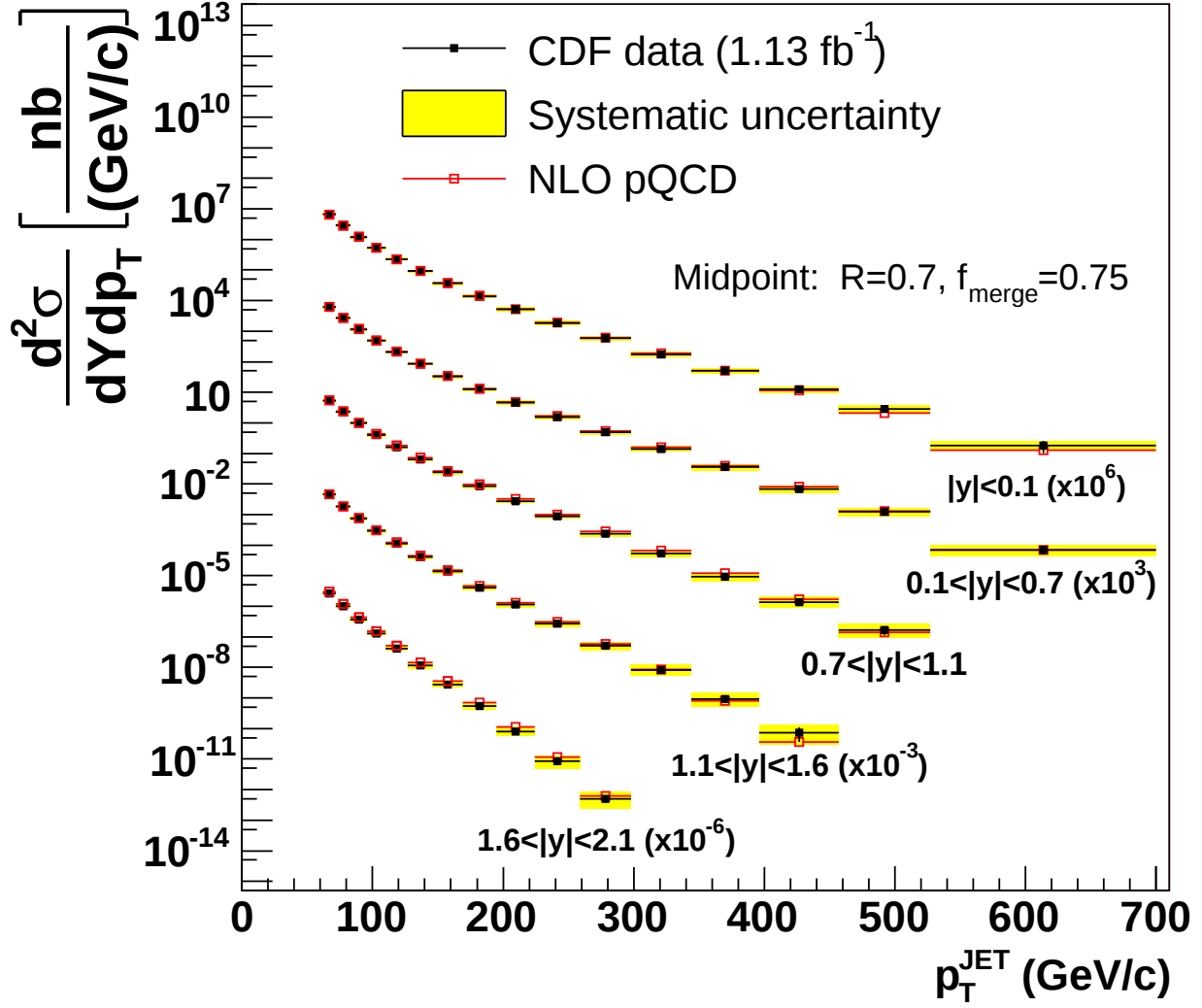
FIG. 15: Inclusive jet cross sections measured at the hadron level using the Midpoint algorithm in five rapidity regions compared to NLO pQCD predictions based on the CTEQ6.1M PDF. The cross sections for the five rapidity regions are scaled by a factor of 10^3 from each other for presentation purposes.
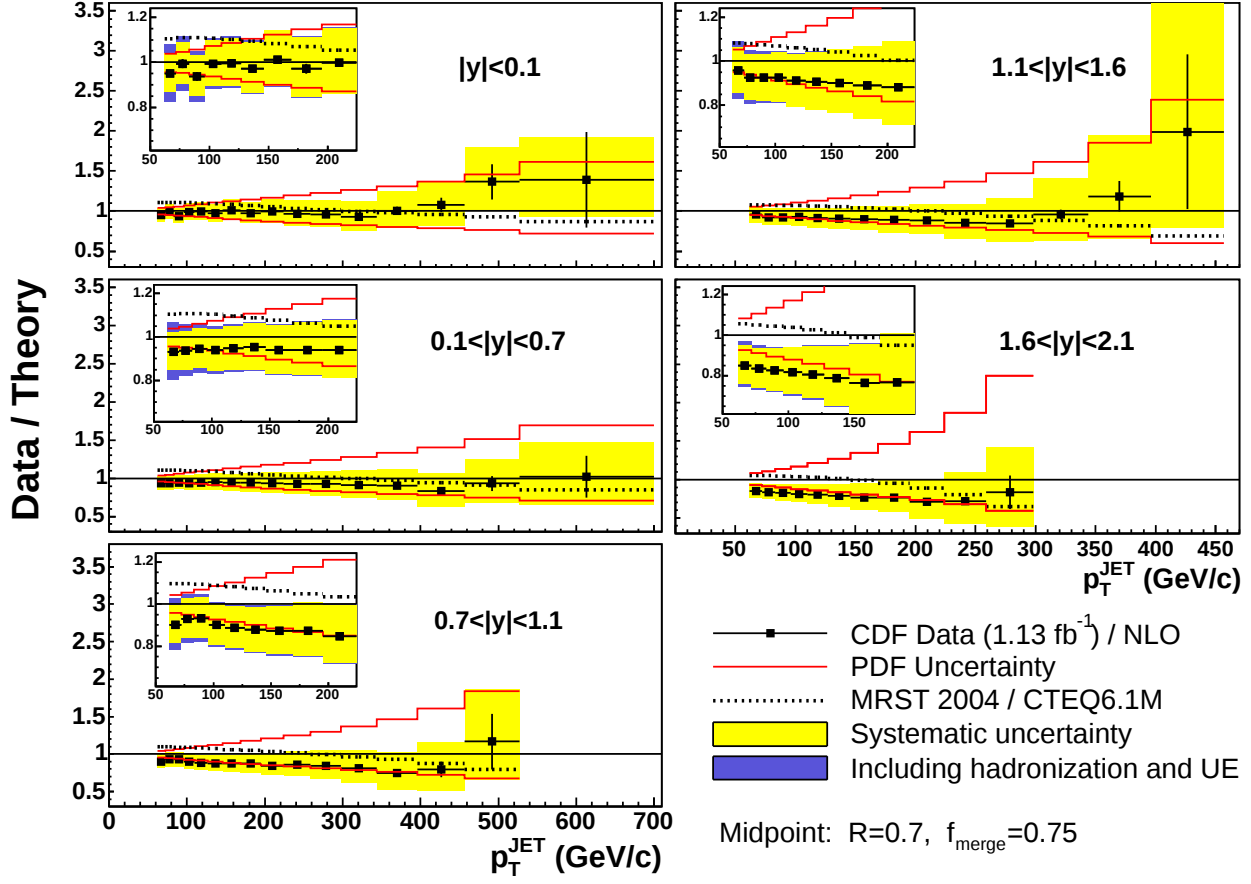
FIG. 16: The ratios of the measured inclusive jet cross sections at the hadron level with the Midpoint jet clustering algorithm to the NLO pQCD predictions (corrected to the hadron level) in five rapidity regions. Also shown are the experimental systematic uncertainties on the measured cross section, the uncertainties in the hadronization and underlying event corrections added in quadrature with the experimental systematic uncertainties, and the PDF uncertainties on the theoretical predictions. The ratios of the theoretical predictions based on the MRST2004 and CTEQ6.1M are shown by the dotted lines.
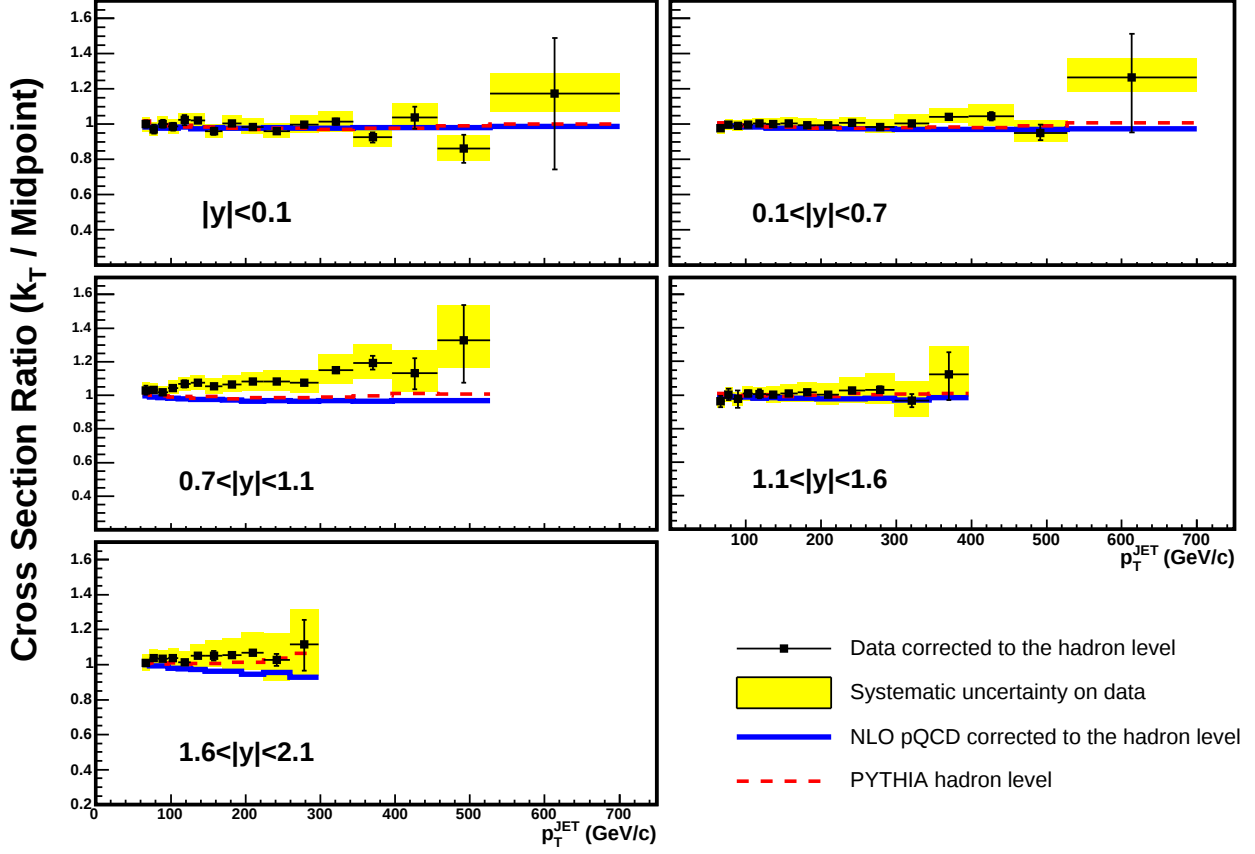
FIG. 17: The ratios of the inclusive jet cross sections measured using the k_T algorithm with $D = 0.7$ [8] to those measured using the Midpoint jet finding algorithm with $R_{cone} = 0.7$ in this paper (points). The systematic uncertainty on the ratio is given as the yellow band. The predictions from NLO pQCD (solid lines) and PYTHIA (dashed lines) for this ratio are also shown.

TABLE II: Relative contributions to the total jet energy scale uncertainty.

p_T (GeV/c)	p_T-independent uncertainty	response to hadrons $p < 12$ GeV/c	response to hadrons $12 < p < 20$ GeV/c	response to hadrons $p > 20$ GeV/c
$62 - 72$	90.0	35.1	16.7	19.7
$72 - 83$	89.8	32.1	17.3	24.8
$83 - 96$	89.1	29.1	17.7	30.1
$96 - 110$	87.7	26.1	16.9	36.6
$110 - 127$	86.2	22.9	16.7	41.9
$127 - 146$	84.1	19.9	15.4	47.9
$146 - 169$	81.8	17.0	14.2	53.1
$169 - 195$	79.7	14.8	12.9	57.1
$195 - 224$	77.5	12.6	11.7	60.8
$224 - 259$	75.6	10.9	10.5	63.7
$259 - 298$	73.6	9.2	9.3	66.4
$298 - 344$	71.9	7.9	8.3	68.5
$344 - 396$	70.1	6.7	7.3	70.6
$396 - 457$	69.0	5.9	6.5	71.9
$457 - 527$	67.7	5.0	5.8	73.2
$527 - 700$	66.4	4.2	5.0	74.5

TABLE III: Systematic uncertainties on the measured inclusive jet differential cross sections from different sources (as discussed in Sec. VI) as a function of p_T for jets in the region $|y| < 0.1$.

		Systematic uncertainties [%] ($|y| < 0.1$)				
p_T (GeV/c)	jet energy scale	dijet p_T balance nominal	dijet p_T balance additional	pileup	unfolding	p_T-spectra	resolution
$62.0 - 72.0$	$+6.7 \\ -6.5$	$+2.3 \\ -1.7$	—	$+1.9 \\ -1.9$	± 3.7	± 0.1	$+3.9 \\ -3.6$
$72.0 - 83.0$	$+7.3 \\ -7.0$	$+1.9 \\ -2.0$	—	$+1.8 \\ -1.7$	± 3.6	± 0.2	$+3.9 \\ -3.6$
$83.0 - 96.0$	$+7.9 \\ -7.5$	$+2.3 \\ -1.7$	—	$+1.7 \\ -1.6$	± 3.5	± 1.0	$+3.9 \\ -3.6$
$96.0 - 110.0$	$+8.6 \\ -8.1$	$+2.4 \\ -2.3$	—	$+1.6 \\ -1.4$	± 3.3	± 0.6	$+4.0 \\ -3.6$
$110.0 - 127.0$	$+9.5 \\ -8.7$	$+2.0 \\ -1.8$	—	$+1.5 \\ -1.3$	± 3.2	± 0.7	$+4.0 \\ -3.6$
$127.0 - 146.0$	$+10.4 \\ -9.5$	$+2.6 \\ -2.4$	—	$+1.3 \\ -1.2$	± 3.1	± 1.5	$+4.1 \\ -3.7$
$146.0 - 169.0$	$+11.5 \\ -10.4$	$+2.6 \\ -1.4$	—	$+1.2 \\ -1.1$	± 2.9	± 1.1	$+4.2 \\ -3.8$
$169.0 - 195.0$	$+12.8 \\ -11.5$	$+3.1 \\ -2.7$	—	$+1.1 \\ -1.1$	± 2.7	± 1.6	$+4.5 \\ -3.9$
$195.0 - 224.0$	$+14.2 \\ -12.6$	$+3.2 \\ -2.5$	—	$+0.9 \\ -1.0$	± 2.5	± 1.2	$+4.8 \\ -4.1$
$224.0 - 259.0$	$+15.9 \\ -14.0$	$+2.8 \\ -2.3$	—	$+0.8 \\ -1.0$	± 2.3	± 1.6	$+5.2 \\ -4.4$
$259.0 - 298.0$	$+17.8 \\ -15.5$	$+3.4 \\ -2.4$	—	$+0.7 \\ -0.9$	± 2.1	± 0.8	$+5.8 \\ -4.9$
$298.0 - 344.0$	$+19.9 \\ -17.3$	$+4.2 \\ -3.4$	—	$+0.5 \\ -0.9$	± 1.9	± 0.2	$+6.6 \\ -5.5$
$344.0 - 396.0$	$+22.4 \\ -19.3$	$+4.0 \\ -2.9$	—	$+0.4 \\ -0.9$	± 1.7	± 0.4	$+7.8 \\ -6.4$
$396.0 - 457.0$	$+25.1 \\ -21.6$	$+5.1 \\ -4.3$	—	$+0.3 \\ -0.9$	± 1.5	± 2.2	$+9.5 \\ -7.7$
$457.0 - 527.0$	$+28.3 \\ -24.2$	$+5.7 \\ -4.7$	—	$+0.1 \\ -0.8$	± 1.4	± 9.3	$+11.7 \\ -9.5$
$527.0 - 700.0$	$+34.0 \\ -29.0$	$+6.0 \\ -4.8$	—	$+0.1 \\ -0.8$	± 1.4	± 19.1	$+16.9 \\ -13.7$

TABLE IV: Systematic uncertainties on the measured inclusive jet differential cross section from different sources (as discussed in Sec. VI) as a function of p_T for jets in the region $0.1 < |y| < 0.7$.

p_T (GeV/c)	jet energy scale	dijet p_T balance nominal	additional	pileup	unfolding	p_T-spectra	resolution
$62.0 - 72.0$	$^{+7.4}_{-7.0}$	$^{+2.2}_{-1.8}$	—	$^{+1.9}_{-1.8}$	± 3.7	± 0.5	$^{+3.5}_{-3.1}$
$72.0 - 83.0$	$^{+7.8}_{-7.4}$	$^{+2.3}_{-1.9}$	—	$^{+1.7}_{-1.7}$	± 3.5	± 0.5	$^{+3.4}_{-3.0}$
$83.0 - 96.0$	$^{+8.3}_{-7.8}$	$^{+2.2}_{-1.9}$	—	$^{+1.6}_{-1.5}$	± 3.4	± 0.5	$^{+3.4}_{-3.0}$
$96.0 - 110.0$	$^{+8.8}_{-8.3}$	$^{+2.4}_{-2.3}$	—	$^{+1.4}_{-1.4}$	± 3.3	± 0.7	$^{+3.3}_{-2.9}$
$110.0 - 127.0$	$^{+9.5}_{-8.9}$	$^{+2.1}_{-1.8}$	—	$^{+1.3}_{-1.3}$	± 3.2	± 0.5	$^{+3.3}_{-2.9}$
$127.0 - 146.0$	$^{+10.3}_{-9.6}$	$^{+2.7}_{-1.9}$	—	$^{+1.2}_{-1.2}$	± 3.0	± 0.6	$^{+3.3}_{-2.8}$
$146.0 - 169.0$	$^{+11.2}_{-10.4}$	$^{+2.8}_{-2.4}$	—	$^{+1.2}_{-1.1}$	± 2.8	± 0.6	$^{+3.4}_{-2.8}$
$169.0 - 195.0$	$^{+12.3}_{-11.4}$	$^{+3.1}_{-2.3}$	—	$^{+1.1}_{-1.1}$	± 2.6	± 0.7	$^{+3.5}_{-2.9}$
$195.0 - 224.0$	$^{+13.7}_{-12.5}$	$^{+3.5}_{-2.7}$	—	$^{+1.0}_{-1.0}$	± 2.5	± 0.4	$^{+3.7}_{-3.0}$
$224.0 - 259.0$	$^{+15.3}_{-13.8}$	$^{+2.7}_{-2.1}$	—	$^{+1.0}_{-1.0}$	± 2.3	± 0.4	$^{+4.1}_{-3.2}$
$259.0 - 298.0$	$^{+17.3}_{-15.4}$	$^{+3.7}_{-2.8}$	—	$^{+1.0}_{-0.9}$	± 2.1	± 0.4	$^{+4.6}_{-3.6}$
$298.0 - 344.0$	$^{+19.6}_{-17.4}$	$^{+4.4}_{-3.2}$	—	$^{+1.0}_{-0.9}$	± 1.9	± 0.2	$^{+5.4}_{-4.2}$
$344.0 - 396.0$	$^{+22.6}_{-19.7}$	$^{+4.6}_{-3.5}$	—	$^{+0.9}_{-0.9}$	± 1.7	± 0.2	$^{+6.6}_{-5.1}$
$396.0 - 457.0$	$^{+26.1}_{-22.5}$	$^{+5.8}_{-4.5}$	—	$^{+0.9}_{-0.8}$	± 1.7	± 0.8	$^{+8.2}_{-6.4}$
$457.0 - 527.0$	$^{+30.6}_{-25.9}$	$^{+7.0}_{-5.4}$	—	$^{+0.9}_{-0.8}$	± 1.7	± 1.0	$^{+10.6}_{-8.2}$
$527.0 - 700.0$	$^{+39.7}_{-32.7}$	$^{+7.1}_{-5.5}$	—	$^{+0.9}_{-0.8}$	± 2.0	± 3.5	$^{+16.2}_{-12.8}$

TABLE V: Systematic uncertainties on the measured inclusive jet differential cross section from different sources (as discussed in Sec. VI) as a function of p_T for jets in the region $0.7 < |y| < 1.1$.

p_T (GeV/c)	jet energy scale	dijet p_T balance nominal	additional	pileup	unfolding	p_T-spectra	resolution
$62.0 - 72.0$	$^{+8.0}_{-7.4}$	$^{+2.1}_{-1.9}$	—	$^{+2.0}_{-1.9}$	± 4.2	± 0.7	$^{+4.0}_{-3.3}$
$72.0 - 83.0$	$^{+8.3}_{-7.8}$	$^{+2.5}_{-2.0}$	—	$^{+1.8}_{-1.7}$	± 4.1	± 0.4	$^{+3.9}_{-3.3}$
$83.0 - 96.0$	$^{+8.7}_{-8.2}$	$^{+2.7}_{-2.0}$	—	$^{+1.7}_{-1.6}$	± 3.9	± 0.7	$^{+3.8}_{-3.2}$
$96.0 - 110.0$	$^{+9.2}_{-8.7}$	$^{+2.0}_{-2.2}$	—	$^{+1.5}_{-1.5}$	± 3.8	± 0.6	$^{+3.8}_{-3.2}$
$110.0 - 127.0$	$^{+9.9}_{-9.3}$	$^{+2.2}_{-1.7}$	—	$^{+1.4}_{-1.4}$	± 3.6	± 0.7	$^{+3.8}_{-3.2}$
$127.0 - 146.0$	$^{+10.8}_{-10.1}$	$^{+2.9}_{-2.1}$	—	$^{+1.3}_{-1.3}$	± 3.4	± 0.7	$^{+3.9}_{-3.2}$
$146.0 - 169.0$	$^{+12.0}_{-11.1}$	$^{+3.1}_{-2.3}$	—	$^{+1.2}_{-1.2}$	± 3.2	± 0.7	$^{+4.1}_{-3.4}$
$169.0 - 195.0$	$^{+13.7}_{-12.4}$	$^{+3.2}_{-2.9}$	—	$^{+1.2}_{-1.1}$	± 3.0	± 0.7	$^{+4.4}_{-3.7}$
$195.0 - 224.0$	$^{+15.8}_{-14.0}$	$^{+3.5}_{-2.6}$	—	$^{+1.1}_{-1.1}$	± 2.8	± 0.7	$^{+4.9}_{-4.1}$
$224.0 - 259.0$	$^{+18.7}_{-16.1}$	$^{+4.1}_{-3.0}$	—	$^{+1.0}_{-1.0}$	± 2.6	± 0.6	$^{+5.8}_{-4.8}$
$259.0 - 298.0$	$^{+22.5}_{-18.7}$	$^{+4.5}_{-3.2}$	—	$^{+1.0}_{-1.0}$	± 2.4	± 0.7	$^{+7.0}_{-5.9}$
$298.0 - 344.0$	$^{+27.6}_{-22.1}$	$^{+5.3}_{-4.0}$	—	$^{+1.0}_{-0.9}$	± 2.3	± 1.2	$^{+8.7}_{-7.4}$
$344.0 - 396.0$	$^{+34.4}_{-26.4}$	$^{+5.9}_{-4.8}$	—	$^{+0.9}_{-0.9}$	± 2.2	± 1.7	$^{+11.2}_{-9.6}$
$396.0 - 457.0$	$^{+43.4}_{-32.1}$	$^{+7.6}_{-6.5}$	—	$^{+0.9}_{-0.8}$	± 2.1	± 2.5	$^{+14.6}_{-12.7}$
$457.0 - 527.0$	$^{+55.4}_{-39.4}$	$^{+10.3}_{-7.4}$	—	$^{+0.9}_{-0.8}$	± 2.3	± 4.6	$^{+19.5}_{-17.1}$

TABLE VI: Systematic uncertainties on the measured inclusive jet differential cross sections from different sources (as discussed in Sec. VI) as a function of p_T for jets in the region $1.1 < |y| < 1.6$.

		dijet p_T balance					
p_T (GeV/c)	jet energy scale	nominal	additional	pileup	unfolding	p_T-spectra	resolution
$62.0 - 72.0$	$+8.5$ -7.8	$+2.4$ -2.0	—	$+2.1$ -1.9	$+3.0$ -2.9	± 5.5	± 0.2
$72.0 - 83.0$	$+9.0$ -8.4	$+2.6$ -2.1	—	$+1.9$ -1.8	$+2.9$ -2.9	± 5.5	± 0.3
$83.0 - 96.0$	$+9.6$ -9.0	$+2.8$ -2.0	—	$+1.8$ -1.7	$+2.9$ -2.8	± 5.4	± 0.4
$96.0 - 110.0$	$+10.5$ -9.8	$+2.4$ -2.3	—	$+1.7$ -1.6	$+2.9$ -2.9	± 5.3	± 0.4
$110.0 - 127.0$	$+11.6$ -10.8	$+2.5$ -2.2	—	$+1.6$ -1.5	$+3.0$ -3.0	± 5.2	± 0.5
$127.0 - 146.0$	$+13.1$ -12.0	$+3.4$ -2.7	—	$+1.5$ -1.5	$+3.2$ -3.2	± 5.1	± 0.6
$146.0 - 169.0$	$+15.2$ -13.5	$+3.5$ -2.6	—	$+1.5$ -1.4	$+3.7$ -3.6	± 4.9	± 0.6
$169.0 - 195.0$	$+18.0$ -15.4	$+4.4$ -3.2	—	$+1.4$ -1.4	$+4.4$ -4.3	± 4.8	± 0.8
$195.0 - 224.0$	$+21.7$ -17.8	$+4.5$ -3.6	$+2.3$ -2.0	$+1.4$ -1.3	$+5.5$ -5.2	± 4.6	± 0.2
$224.0 - 259.0$	$+26.6$ -20.7	$+5.4$ -4.0	$+5.4$ -4.5	$+1.4$ -1.3	$+7.1$ -6.6	± 4.4	± 1.1
$259.0 - 298.0$	$+33.1$ -24.6	$+5.9$ -5.0	$+9.4$ -8.7	$+1.4$ -1.3	$+9.5$ -8.6	± 4.2	± 0.2
$298.0 - 344.0$	$+41.8$ -29.4	$+8.0$ -5.8	$+16.2$ -14.5	$+1.4$ -1.3	$+12.9$ -11.4	± 4.0	± 3.3
$344.0 - 396.0$	$+53.4$ -35.6	$+9.8$ -6.5	$+29.6$ -21.8	$+1.4$ -1.3	$+17.7$ -15.3	± 3.8	± 10.2
$396.0 - 457.0$	$+68.8$ -43.5	$+12.4$ -7.6	$+52.2$ -26.5	$+1.4$ -1.2	$+24.4$ -20.7	± 3.5	± 21.7

TABLE VII: Systematic uncertainties on the measured inclusive jet differential cross sections from different sources (as discussed in Sec. VI) as a function of p_T for jets in the region $1.6 < |y| < 2.1$.

		dijet p_T balance					
p_T (GeV/c)	jet energy scale	nominal	additional	pileup	unfolding	p_T-spectra	resolution
$62.0 - 72.0$	$+9.9$ -9.0	$+2.6$ -2.3	—	$+2.5$ -2.4	± 4.1	± 0.2	$+2.5$ -2.0
$72.0 - 83.0$	$+10.8$ -9.9	$+2.8$ -2.5	—	$+2.2$ -2.1	± 3.7	± 0.1	$+2.5$ -2.0
$83.0 - 96.0$	$+12.0$ -11.0	$+3.5$ -2.6	—	$+2.0$ -1.9	± 3.3	± 0.2	$+2.5$ -2.0
$96.0 - 110.0$	$+13.8$ -12.3	$+3.4$ -2.8	—	$+1.9$ -1.9	± 2.9	± 0.3	$+2.6$ -2.0
$110.0 - 127.0$	$+16.1$ -14.1	$+3.6$ -3.2	—	$+1.9$ -1.8	± 2.7	± 0.3	$+2.8$ -2.2
$127.0 - 146.0$	$+19.3$ -16.4	$+4.3$ -3.8	—	$+1.9$ -1.9	± 2.7	± 0.3	$+3.2$ -2.5
$146.0 - 169.0$	$+23.8$ -19.5	$+4.7$ -3.5	—	$+2.0$ -1.9	± 2.9	± 0.2	$+3.8$ -3.0
$169.0 - 195.0$	$+30.0$ -23.5	$+6.2$ -6.6	$+4.9$ -5.1	$+2.1$ -2.1	± 3.7	± 0.3	$+4.8$ -3.8
$195.0 - 224.0$	$+38.1$ -28.7	$+8.1$ -5.2	$+10.1$ -7.3	$+2.3$ -2.2	± 5.0	± 0.4	$+6.2$ -5.0
$224.0 - 259.0$	$+49.2$ -35.6	$+11.5$ -7.8	$+20.7$ -13.4	$+2.5$ -2.4	± 7.3	± 1.9	$+8.2$ -6.7
$259.0 - 298.0$	$+64.1$ -44.7	$+14.8$ -11.5	$+27.9$ -19.7	$+2.8$ -2.5	± 11.0	± 7.4	$+11.1$ -9.2

TABLE VIII: Measured inclusive jet cross sections as a function of p_T for jets in the region $|y| < 0.1$ together with the statistical (*stat.*) and systematic (*sys.*) uncertainties. The bin-by-bin parton-to-hadron-level ($C_{p \to h}$) corrections are also shown.

p_T (GeV/c)	$\sigma \pm (stat.) \pm (sys.)$ [nb/(GeV/c)]	$C_{p \to h}$
$62 - 72$	$(6.68 \pm 0.11^{+0.61}_{-0.58}) \times 10^0$	1.072 ± 0.107
$72 - 83$	$(2.95 \pm 0.06^{+0.28}_{-0.27}) \times 10^0$	1.054 ± 0.086
$83 - 96$	$(1.20 \pm 0.02^{+0.12}_{-0.11}) \times 10^0$	1.040 ± 0.069
$96 - 110$	$(5.38 \pm 0.05^{+0.56}_{-0.53}) \times 10^{-1}$	1.028 ± 0.055
$110 - 127$	$(2.28 \pm 0.03^{+0.25}_{-0.23}) \times 10^{-1}$	1.020 ± 0.043
$127 - 146$	$(9.18 \pm 0.12^{+1.10}_{-1.01}) \times 10^{-2}$	1.013 ± 0.033
$146 - 169$	$(3.78 \pm 0.05^{+0.49}_{-0.44}) \times 10^{-2}$	1.007 ± 0.024
$169 - 195$	$(1.38 \pm 0.03^{+0.20}_{-0.18}) \times 10^{-2}$	1.003 ± 0.017
$195 - 224$	$(5.30 \pm 0.06^{+0.82}_{-0.73}) \times 10^{-3}$	1.000 ± 0.012
$224 - 259$	$(1.83 \pm 0.02^{+0.31}_{-0.27}) \times 10^{-3}$	0.998 ± 0.008
$259 - 298$	$(5.93 \pm 0.11^{+1.13}_{-0.98}) \times 10^{-4}$	0.996 ± 0.004
$298 - 344$	$(1.75 \pm 0.06^{+0.38}_{-0.33}) \times 10^{-4}$	0.996 ± 0.002
$344 - 396$	$(5.06 \pm 0.25^{+1.22}_{-1.04}) \times 10^{-5}$	0.996 ± 0.000
$396 - 457$	$(1.24 \pm 0.10^{+0.34}_{-0.29}) \times 10^{-5}$	0.996 ± 0.001
$457 - 527$	$(2.80 \pm 0.45^{+0.87}_{-0.74}) \times 10^{-6}$	0.997 ± 0.002
$527 - 700$	$(1.81 \pm 0.78^{+0.70}_{-0.59}) \times 10^{-7}$	1.000 ± 0.001

TABLE IX: Measured inclusive jet cross sections as a function of p_T for jets in the region $0.1 < |y| < 0.7$ together with the statistical (*stat.*) and systematic (*sys.*) uncertainties. The bin-by-bin parton-to-hadron-level ($C_{p \to h}$) corrections are also shown.

p_T (GeV/c)	$\sigma \pm (stat.) \pm (sys.)$ [nb/(GeV/c)]	$C_{p \to h}$
$62 - 72$	$(6.28 \pm 0.04^{+0.59}_{-0.56}) \times 10^0$	1.072 ± 0.108
$72 - 83$	$(2.70 \pm 0.02^{+0.26}_{-0.25}) \times 10^0$	1.055 ± 0.088
$83 - 96$	$(1.15 \pm 0.01^{+0.11}_{-0.11}) \times 10^0$	1.041 ± 0.071
$96 - 110$	$(4.88 \pm 0.03^{+0.51}_{-0.48}) \times 10^{-1}$	1.030 ± 0.057
$110 - 127$	$(2.07 \pm 0.01^{+0.22}_{-0.21}) \times 10^{-1}$	1.022 ± 0.045
$127 - 146$	$(8.50 \pm 0.04^{+0.98}_{-0.91}) \times 10^{-2}$	1.015 ± 0.035
$146 - 169$	$(3.30 \pm 0.01^{+0.41}_{-0.38}) \times 10^{-2}$	1.010 ± 0.027
$169 - 195$	$(1.24 \pm 0.01^{+0.17}_{-0.15}) \times 10^{-2}$	1.006 ± 0.020
$195 - 224$	$(4.54 \pm 0.02^{+0.67}_{-0.61}) \times 10^{-3}$	1.003 ± 0.014
$224 - 259$	$(1.56 \pm 0.01^{+0.25}_{-0.23}) \times 10^{-3}$	1.002 ± 0.010
$259 - 298$	$(4.93 \pm 0.04^{+0.91}_{-0.80}) \times 10^{-4}$	1.001 ± 0.006
$298 - 344$	$(1.42 \pm 0.02^{+0.30}_{-0.26}) \times 10^{-4}$	1.000 ± 0.003
$344 - 396$	$(3.54 \pm 0.08^{+0.85}_{-0.73}) \times 10^{-5}$	1.001 ± 0.001
$396 - 457$	$(6.87 \pm 0.34^{+1.93}_{-1.64}) \times 10^{-6}$	1.001 ± 0.000
$457 - 527$	$(1.22 \pm 0.13^{+0.40}_{-0.34}) \times 10^{-6}$	1.003 ± 0.001
$527 - 700$	$(7.08 \pm 1.89^{+3.08}_{-2.52}) \times 10^{-8}$	1.005 ± 0.001

TABLE X: Measured inclusive jet cross sections as a function of p_T for jets in the region $0.7 < |y| < 1.1$ together with the statistical (*stat.*) and systematic (*sys.*) uncertainties. The bin-by-bin parton-to-hadron-level ($C_{p \to h}$) corrections are also shown.

p_T (GeV/c)	$0.7 < |y| < 1.1$ $\sigma \pm (stat.) \pm (sys.)$ [nb/(GeV/c)]	$C_{p \to h}$
$62 - 72$	$(5.32 \pm 0.04^{+0.55}_{-0.50}) \times 10^{0}$	1.061 ± 0.098
$72 - 83$	$(2.32 \pm 0.02^{+0.24}_{-0.23}) \times 10^{0}$	1.048 ± 0.081
$83 - 96$	$(9.83 \pm 0.12^{+1.05}_{-0.99}) \times 10^{-1}$	1.038 ± 0.067
$96 - 110$	$(3.98 \pm 0.02^{+0.44}_{-0.41}) \times 10^{-1}$	1.031 ± 0.055
$110 - 127$	$(1.62 \pm 0.01^{+0.19}_{-0.17}) \times 10^{-1}$	1.024 ± 0.046
$127 - 146$	$(6.34 \pm 0.04^{+0.78}_{-0.73}) \times 10^{-2}$	1.019 ± 0.037
$146 - 169$	$(2.37 \pm 0.02^{+0.32}_{-0.29}) \times 10^{-2}$	1.015 ± 0.030
$169 - 195$	$(8.41 \pm 0.08^{+1.27}_{-1.14}) \times 10^{-3}$	1.012 ± 0.024
$195 - 224$	$(2.79 \pm 0.02^{+0.48}_{-0.42}) \times 10^{-3}$	1.010 ± 0.020
$224 - 259$	$(8.78 \pm 0.10^{+1.78}_{-1.52}) \times 10^{-4}$	1.008 ± 0.016
$259 - 298$	$(2.35 \pm 0.03^{+0.57}_{-0.47}) \times 10^{-4}$	1.007 ± 0.013
$298 - 344$	$(5.37 \pm 0.12^{+1.59}_{-1.28}) \times 10^{-5}$	1.007 ± 0.011
$344 - 396$	$(9.30 \pm 0.53^{+3.41}_{-2.66}) \times 10^{-6}$	1.006 ± 0.010
$396 - 457$	$(1.35 \pm 0.17^{+0.63}_{-0.47}) \times 10^{-6}$	1.007 ± 0.009
$457 - 527$	$(1.63 \pm 0.52^{+0.97}_{-0.71}) \times 10^{-7}$	1.007 ± 0.008

TABLE XI: Measured inclusive jet cross sections as a function of p_T for jets in the region $1.1 < |y| < 1.6$ together with the statistical (*stat.*) and systematic (*sys.*) uncertainties. The bin-by-bin parton-to-hadron-level ($C_{p \to h}$) corrections are also shown.

p_T (GeV/c)	$1.1 < |y| < 1.6$ $\sigma \pm (stat.) \pm (sys.)$ [nb/(GeV/c)]	$C_{p \to h}$
$62 - 72$	$(4.57 \pm 0.04^{+0.50}_{-0.47}) \times 10^{0}$	1.058 ± 0.095
$72 - 83$	$(1.81 \pm 0.02^{+0.21}_{-0.19}) \times 10^{0}$	1.042 ± 0.076
$83 - 96$	$(7.39 \pm 0.09^{+0.88}_{-0.83}) \times 10^{-1}$	1.029 ± 0.059
$96 - 110$	$(2.96 \pm 0.02^{+0.37}_{-0.35}) \times 10^{-1}$	1.020 ± 0.046
$110 - 127$	$(1.13 \pm 0.01^{+0.15}_{-0.14}) \times 10^{-1}$	1.013 ± 0.035
$127 - 146$	$(4.09 \pm 0.03^{+0.61}_{-0.56}) \times 10^{-2}$	1.007 ± 0.025
$146 - 169$	$(1.38 \pm 0.01^{+0.23}_{-0.21}) \times 10^{-2}$	1.003 ± 0.017
$169 - 195$	$(4.13 \pm 0.06^{+0.81}_{-0.70}) \times 10^{-3}$	1.000 ± 0.011
$195 - 224$	$(1.15 \pm 0.01^{+0.27}_{-0.22}) \times 10^{-3}$	0.998 ± 0.006
$224 - 259$	$(2.66 \pm 0.07^{+0.76}_{-0.60}) \times 10^{-4}$	0.997 ± 0.002
$259 - 298$	$(5.02 \pm 0.16^{+1.81}_{-1.39}) \times 10^{-5}$	0.997 ± 0.001
$298 - 344$	$(8.27 \pm 0.51^{+3.88}_{-2.89}) \times 10^{-6}$	0.997 ± 0.003
$344 - 396$	$(9.36 \pm 1.51^{+5.97}_{-4.17}) \times 10^{-7}$	0.998 ± 0.005
$396 - 457$	$(7.17 \pm 3.49^{+6.25}_{-4.30}) \times 10^{-8}$	1.000 ± 0.005

TABLE XII: Measured inclusive jet cross sections as a function of p_T for jets in the region $1.6 < |y| < 2.1$ together with the statistical (*stat.*) and systematic (*sys.*) uncertainties. The bin-by-bin parton-to-hadron-level ($C_{p \to h}$) corrections are also shown.

	$1.6 < |y| < 2.1$	
p_T	$\sigma \pm (stat.) \pm (sys.)$	$C_{p \to h}$
(GeV/c)	[nb/(GeV/c)]	
$62 - 72$	$(2.66 \pm 0.02^{+0.31}_{-0.28}) \times 10^0$	1.038 ± 0.079
$72 - 83$	$(1.00 \pm 0.01^{+0.12}_{-0.11}) \times 10^0$	1.028 ± 0.062
$83 - 96$	$(3.65 \pm 0.02^{+0.48}_{-0.44}) \times 10^{-1}$	1.019 ± 0.048
$96 - 110$	$(1.27 \pm 0.01^{+0.19}_{-0.17}) \times 10^{-1}$	1.013 ± 0.038
$110 - 127$	$(4.12 \pm 0.04^{+0.70}_{-0.61}) \times 10^{-2}$	1.008 ± 0.030
$127 - 146$	$(1.15 \pm 0.01^{+0.23}_{-0.20}) \times 10^{-2}$	1.004 ± 0.024
$146 - 169$	$(2.78 \pm 0.06^{+0.70}_{-0.56}) \times 10^{-3}$	1.001 ± 0.021
$169 - 195$	$(5.44 \pm 0.10^{+1.71}_{-1.34}) \times 10^{-4}$	1.000 ± 0.019
$195 - 224$	$(7.95 \pm 0.22^{+3.20}_{-2.45}) \times 10^{-5}$	0.999 ± 0.019
$224 - 259$	$(8.41 \pm 0.59^{+4.38}_{-3.46}) \times 10^{-6}$	0.998 ± 0.019
$259 - 298$	$(5.08 \pm 1.34^{+3.57}_{-2.74}) \times 10^{-7}$	0.998 ± 0.021